remote sensing

MDPI

Article

Glacier Changes in India's Dhauliganga Catchment over the Past Two Decades

Nauman Ali [1,2], Qinghua Ye [1,*], Xueqin Zhang [3], Xinhui Ji [1,2], Yafan Hu [1,2], Liping Zhu [1] and Arslan Ali [4]

[1] State Key Laboratory Tibetan Plateau Earth System, Environment and Resources (TPESER), Institute of Tibetan Plateau Research, Chinese Academy of Sciences, Beijing 100101, China
[2] Institute of Tibetan Plateau Research, University of Chinese Academy of Sciences, Beijing 100049, China
[3] Institute of Geographic Sciences and Natural Resources Research, Chinese Academy of Sciences, Beijing 100101, China
[4] The State Key Laboratory of Information Engineering in Surveying, Mapping and Remote Sensing, Wuhan University, Wuhan 430079, China
* Correspondence: yeqh@itpcas.ac.cn

Abstract: The rapid melting of glaciers has led to severe glacial-hydrological hazards in the Himalayas. An extreme example occurred on 7 February 2021, when a catastrophic mass flow descended from the Ronti glacier at Chamoli, Indian Himalaya, causing widespread devastation, with more than 200 people killed or missing, as well as severe damage to four hydropower projects. To disclose what happened to the Ronti glacier over the past several decades, here, we focused on glacier changes in the Dhauliganga catchment in Uttarakhand, India, over the past two decades. Another five glaciers in the catchment were also studied to map the regional detailed glacier changes. Our achievements are summarized as follows. (1) Based on Landsat images, we constructed two glacier inventories for the catchment in 2001 and 2020. We mapped nearly 413 debris-free glaciers in the catchment between 2001 and 2020 and analyzed the glacier area change at basin and altitude levels. (2) Debris-free glacier area decreased from 477.48 ± 35.23 km^2 in 2001 to 418.52 ± 36.18 km^2 in 2020, with a reduction of 58.95 km^2 or 12.35% over the past two decades. (3) The geodetic mass balance was −0.27± 0.10 m w.e.a^{-1}, with a glacier mass change of −0.12 Gt. a^{-1} from 2000 to 2013. Based on the surface elevation difference between the Ice, Cloud, and land Elevation Satellite 2 (ICESat-2) footprints (acquired from 2018 to 2021) and the National Aeronautics and Space Administration (NASA) DEM from 2000 to 2021, the average glacier geodetic mass balance was −0.22 ± 0.005 m w.e.a^{-1}, and glacier mass change was −0.10 Gt a^{-1}. (4) Our results were cross verified by available published elevation difference datasets covering multiple temporal periods, where mass balance was by −0.22 ± 0.002 m w.e.a^{-1} from 1975 to 2000 and −0.28 ± 0.0001 w.e.a^{-1} from 2000 to 2020. (5) Glacier 1 and Glacier 2, the two largest glaciers in the catchment, experienced a decreasing melt rate from 2000 to 2020, while Glacier 3, Glacier 4, and Glacier 5 demonstrated an increasing melt rate. However, Glacier 6, also known as the collapsed Ronti glacier, had a negative mass balance of −0.04 m w.e.a^{-1} from 2000 to 2005 and turned positive from 2005 onward with 0.06 m w.e.a^{-1} from 2005 to 2010, 0.19 m w.e.a^{-1} from 2010 to 2015, and 0.32 m w.e.a^{-1} from 2015 to 2020. We postulate that the Ronti glacier collapsed solely because of the significant mass accumulation observed between 3700 to 5500 m a.s.l. Our study helps to understand the collapsed glacier's mass changes over the past two decades and highlights the necessity to monitor mass-gaining glaciers from space to forecast the risks of disasters.

Keywords: glacier changes; geodetic mass balance; ICESat-2; NASADEM; SRTM; Dhauliganga catchment; India; Central Himalaya

Citation: Ali, N.; Ye, Q.; Zhang, X.; Ji, X.; Hu, Y.; Zhu, L.; Ali, A. Glacier Changes in India's Dhauliganga Catchment over the Past Two Decades. *Remote Sens.* **2022**, *14*, 5692. https://doi.org/10.3390/rs14225692

Academic Editor: Ireneusz Sobota

Received: 11 August 2022
Accepted: 3 November 2022
Published: 10 November 2022

1. Introduction

High mountain Asia (HMA) hosts the largest concentration of glaciers outside the polar region [1], earning it the well-deserved moniker of being the Third Pole [2]. Glacier change studies based on satellite data reveal that HMA experienced significant glacier loss in recent

decades, although spatial heterogeneities exist [3–6]. Since HMA is home to a population of 1.5 billion inhabitants [2], glaciers and melting glaciers have significant implications as they deliver freshwater downstream. Glacier meltwater is used in hydropower and agricultural sectors [7]. However, despite the salutary benefits of glacier melting, glacier change may lead to multiple disasters, such as outburst floods, avalanches, landslides, and mudslides [8].

Due to harsh climatic conditions, poor logistics, and remote locations, in-situ studying glaciers in HMA is costly and complex. Remote sensing techniques offer valuable alternatives. Regional and local glacier mapping studies have been conducted across HMA using different methods and satellite sensors [1,3,9–11]. The first Chinese glacier inventory (CGI-1), conducted from 1978 to 2002, mapped 46,377 glaciers covering an area of 59,425 km^2 across the Chinese territories [12]. The second Chinese glacier inventory (CGI-2) used Landsat 4 and 5 Thematic Mapper (TM) and the Landsat 7 Enhanced Thematic Mapper Plus (ETM+) images from 2006 to 2010 and mapped 42,370 debris-free glaciers covering 43,086.8 km^2 and 1723 debris cover glaciers covering 1493.7 km^2 [9]. Using Landsat images, the GAMDAM glacier inventory 2015 (GGI-15) spanned from 1999 to 2003 and mapped 87,084 glaciers covering an area of 91,263 $\pm$ 13,689 km^2 in Asia [10]. Following the GGI-15, GAMDAM glacier inventory 2018 (GGI-18) [11] extended the temporal coverage from 1990 to 2010 and mapped 134,770 glaciers covering 100,693 $\pm$ 11,790 km^2. The Randolph Glacier Inventory (RGI) is a global inventory curated from multiple glacier inventories, including CGIs. Its most recent version is RGI V.6.0, detailing 95,536 glaciers with an area of 97,605.92 km^2 in HMA [1]. Ye and others used Landsat images and a manual delineation method to obtain three epochs of glacier coverage datasets in the Tibetan Plateau over the past 40 years, i.e., Tibetan Plateau Glacier inventory (TPG) 1976, TPG2001, and TPG2013 [3]. The Indus Ganga and Brahmaputra (IGB) glacier inventory covers the Indus, Ganges, and Brahmaputra basins from 2004–2007, with Resourcesat-1 images defining 32,392 glaciers with an area of 71,182.18 km^2 [13]. Due to uncertainties from seasonal snow and cloud cover, mountain shadow effects, rapid glacier changes, and limited satellite images, these and other glacier inventories should be updated periodically or un-periodically.

Studies of regional glaciers suggest that HMA glaciers have been retreating since the mid-19th century [14]. The minimum mass loss for HMA glaciers was reported as -4 ± 20 Gt a^{-1} from 2003 to 2010 [15], with the maximum mass loss of -28 ± 6 Gt a^{-1} from 2003 to 2019 [16]. Despite the spatial heterogeneities in the northwestern Himalayas, the Karakoram, and the Kunlun regions, HMA glaciers have been experiencing significant mass loss since the 21st century [4–6,15,17,18].

The above data sets and analyses demonstrate that HMA glaciers are rapidly melting, leading to a greater magnitude and increased frequency of glacial-hydrological hazards over the past two decades [19]. For example, Uttarakhand, India, located in the central Himalayas, experienced increased climatological hazards [20]. The most extreme event occurred on 7 February, 2021, when a large piece of snow and ice-covered rock broke off the Ronti glacier (Figure 1b,c) at 5600 m a.s.l. on the northern slopes of Trishul mountain [21]. The total volume of the collapsed mass was approximately 23 $\times$ 10^6 m^3 [21] or 27 $\times$ 10^6 m^3 [22]. In addition, severe flood impacted the Ronti Gad, Rishiganga, and Dhauliganga valleys in the Chamoli district of Uttarakhand, resulting in the disappearance or death of over 200 people and extensive infrastructure damage to hydropower installations [22]. Four hydropower projects were adversely impacted, including two operational hydropower plants (i.e., Rishi Ganga Hydropower Project 13.2 MW and Vishnuprayag Hydro Electric Project 400 MW) and two plants under construction (i.e., Tapovan Vishnugad Hydropower Project 520 MW and Vishnugad Pipalkoti Hydro Electric Project 444 MW) [23].

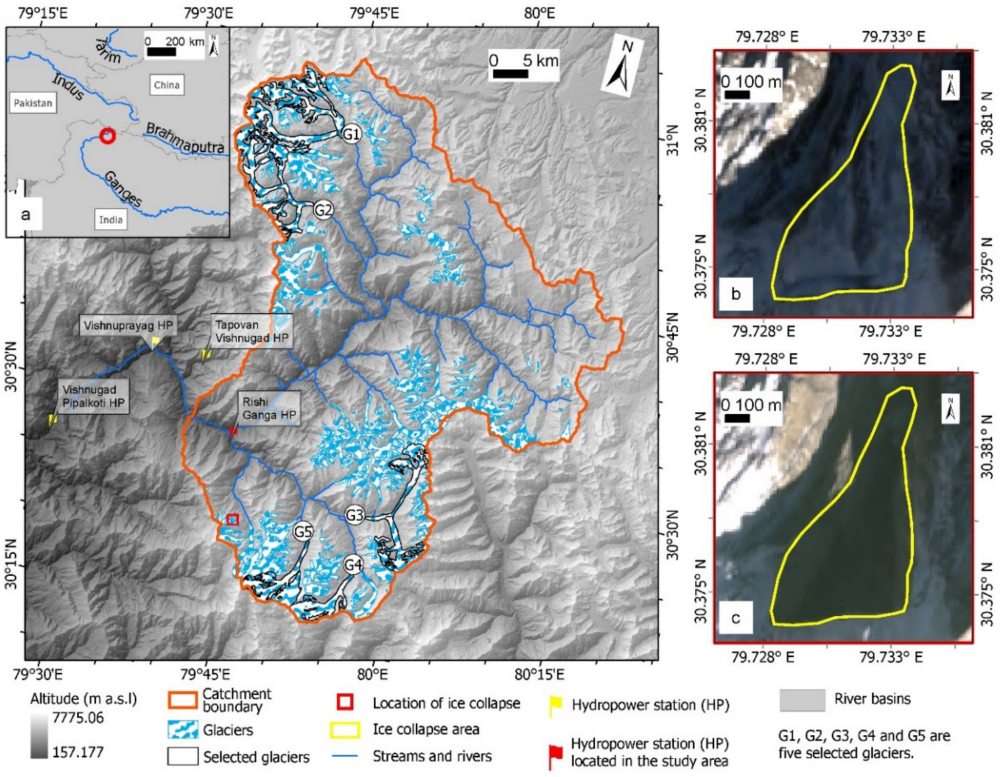

Figure 1. Topographic features and the distribution of glaciers and hydropower stations in the Dhauliganga catchment, Uttarakhand, India. (**a**) Location of Dhauliganga catchment. (**b**) Visible cracks in the Ronti Glacier were presented on the Sentinel 2 image on 31 January 2021. (**c**) The collapsed area of the Ronti glacier in the Sentinel 2 image on 10 February 2021.

In light of the Ronti collapse and the related disasters, we investigate the glacier changes in the Dhauliganga catchment. The aims of this study are: (i) to analyze the area change of debris-free glaciers between 2001 to 2020, (ii) to calculate glacier surface elevation change and geodetic mass balance for debris-free and debris-cover glaciers from 2000 to 2021, (iii) to compare the glacier surface elevation change and geodetic mass balance from 1975 to 2020, and (iv) to analyze glacier surface elevation change, geodetic mass balance, and mass change for six selected glaciers, including the collapsed Ronti glacier.

2. Study Area

The study area covers Dhauliganga and Rishiganga catchments, collectively called the Dhauliganga catchment, located in India's northern hilly state of Uttarakhand, the Central Himalayan region (Figure 1a). The Dhauliganga catchment boundary was delineated by taking the destroyed Tapovan hydropower plant as the outlet. The catchment ranges from approximately 1780 m a.s.l. to 7800 m a.s.l. and exhibits a highly complex terrain, including the mountain peaks of Nanda Devi at 7816 m, Kamet at 7272 m, Mana I at 7274 m, Trisul at 7120 m, Tirsuli at 7074 m, Rishi Pahar at 6992 m, and Kalanka at 6931 m in height. Moreover, the catchment covers a total area of 2896.54 km^2, with 250 glaciers covering 431.63 km^2 [1], 15% of the study area. Glaciers in the catchment, influenced mainly by the Indian monsoon system, are shrinking remarkably due to the warming climate [24], leading to increased glacial lakes [25].

Here, we selected six glaciers to analyze the surface elevation change and geodetic mass balance in the Dhauliganga catchment (Figure 1a and Table 1), including the collapsed Ronti Glacier (Figure 1b,c), the sixth glacier with no ICESat-2 footprints over it. Another five glaciers were selected based on size (i.e., more giant glaciers), aspect (glaciers facing different directions), and the number of ICESat-2 footprints overlayed (Figure 2).

Table 1. Details about the six selected glaciers in the study.

Glacier Number	Glaciers Name	GGI-18 GLIMS ID	Aspect	Glacier Area (km^2)	Number of ICESat-2 Footprints
Glacier 1	Raikana Glacier Ganesh Glacier Uttari Rikana Glacier Puribi Kamet Glacier	G079664E30918N	East	61.05	7664
Glacier 2	Bankund Glacier	G079652E30828N	East	45.55	5268
Glacier 3	Rishi Glacier Uttari Nanda Devi Glacier	G079986E30444N	West	38.71	3578
Glacier 4	Mrigthuni Dakkhni Rishi Glacier	G079897E30298N	North	20.66	1872
Glacier 5	Trisul Glacier	G079897E30298N	North	28.66	2997
Glacier 6	Ronti Glacier	G079733E30379N	North	0.47	*

* There were no ICESat-2 footprints over the Ronti Glacier.

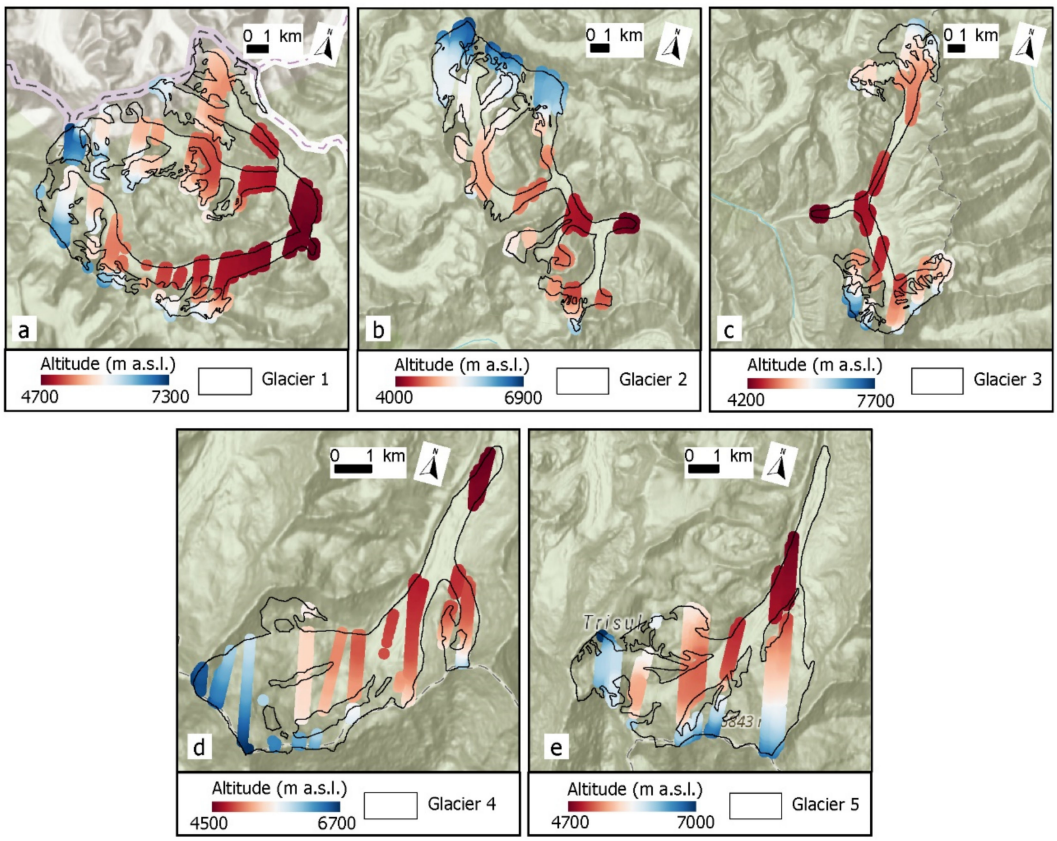

Figure 2. The distribution of ICESat-2 ATL06 footprints over the selected five glaciers. (**a**) Glacier 1 is compounded by four glaciers, i.e., Raikana Glacier, Ganesh Glacier, Uttari Rikana Glacier, and Puribi Kamet Glacier. (**b**) Glacier 2 is Bankund Glacier. (**c**) Glacier 3 is comprised of Rishi Glacier and Uttri Nanda Devi Glacier. (**d**) Glacier 4 is Mrigthuni Dakkhni Rishi Glacier. (**e**) Glacier 5 is Trisul Glacier.

3. Materials and Methods

3.1. Materials

We used Landsat imageries to analyze glacier area change. Additionally, glacier surface elevation change was studied using freely available DEMs, ICESat-2 ATL06 data, and surface elevation difference datasets (Table 2).

Table 2. Datasets used in this study.

Datasets	Time	Spatial Resolution	Source/Reference
Landsat 5 TM	9 October 1994	30 m	https://earthexplorer.usgs.gov/ (accessed on 23 April 2021)
Landsat 7 ETM+	8 October 2001	30 m	https://earthexplorer.usgs.gov/ (accessed on 23 April 2021)
Landsat 8 OLI	16 October 2020	30 m	https://earthexplorer.usgs.gov/ (accessed on 23 April 2021)
SRTM-C band	11–22 February 2000	30 m	https://search.earthdata.nasa.gov/ (accessed on 2 May 2021)
SRTM-X band	11–22 February 2000	90 m	https://geoservice.dlr.de/ (accessed on 15 May 2021)
NASA DEM	11–22 February 2000	30 m	https://search.earthdata.nasa.gov/ (accessed on 5 April 2022)
TanDEM-X	December 2010 to 2015	90 m	https://geoservice.dlr.de/ (accessed on 15 May 2021)
ICESat-2 ATL06	25 October 2018–20 December 2021	~17 m	https://search.earthdata.nasa.gov/ (accessed on 5 April 2022)
DH/DTM	1975–2016	30 m	[26]
DH/DTB	2000–2016	30 m	[4]
DH/DTH	2000–2020	100 m	[27]
Climate data	1950–2021	9 km	[28,29]

3.1.1. Landsat Images

To establish the glacier inventory in the Dhauliganga catchment, we used satellite images from Landsat 5 TM, Landsat 7 ETM+, and Landsat 8 Operational Land Imager (OLI) (Table 2). In addition, images with minimal snow and cloud cover were utilized to mitigate the potential uncertainties of seasonal snow and cloud cover. The Landsat Collection 2 surface reflectance images were extracted automatically on the Google Earth Engine (GEE) platform, which was geometrically and radiometrically corrected.

3.1.2. DEM Data

Glacier mass balance was derived from publicly available DEMs, including NASA DEM, TanDEM-X, and SRTM DEM (Table 3). NASA DEM, released in 2020, was generated by reprocessing the original SRTM signal data [30]. To reduce voids and improve vertical accuracy, NASA DEM employed updated interferometric unwrapping algorithms and data from ICESat GLAS and ASTER. Here, we used the NASA DEM HGT product referenced to the EGM96 geoid.

Table 3. DEMs used in the study.

Dataset	Horizontal Reference	Vertical Datum	Period
NASA DEM	WGS 1984	EGM96 Geoid	2000
TanDEM-X	WGS 1984	Ellipsoid WGS 1984	2013
SRTM-C band	WGS 1984	EGM96 Geoid	2000
SRTM-X band	WGS 1984	Ellipsoid WGS 1984	2000

TanDEM-X DEM was obtained from December 2010 to December 2015 [31]. For the requirement of the representation year, we defined 2013 as the median of start and end dates. TanDEM-X is referenced to the WGS84 ellipsoid and has an excellent absolute linear height error below 2 m at a confidence of 90% [32]. Here, we used the freely available 90 m TanDEM-X DEM, then resampled it to 30 m.

The Shuttle Radar Topography Mission (SRTM), a DEM V3 product (SRTM DEM V3) [33], is provided by NASA's Jet Propulsion Laboratory and is available in the GEE.

SRTM DEM V3 is a void-filled product with a spatial resolution of 1 arc-second (approximately 30 m). The SRTM DEM V3 has two bands of C and X with the horizontal referencing of WGS84, the vertical referencing of EGM96 geoid for the C band, and of WGS84 ellipsoid for the X band [33,34].

3.1.3. ICESat-2 Data

We employed available ICESat-2 L3A Land Ice Height V005 (ATL06) products. The available ICESat-2 footprints were used from 25 October 2018 to 20 December 2021. Both horizontal and vertical referencing were WGS84 [35,36]. To obtain high-quality results, we selected footprints with a "Quality flag" 0. Over the study catchment, 274,510 footprints were used to investigate glacier surface elevation change and geodetic mass balance. Fifty-two thousand seven hundred forty footprints covered the glacial region.

3.1.4. Datasets of Surface Elevation Difference

We adopted the available elevation difference datasets to estimate glacier surface elevation change and geodetic mass balance in the study area from 1975 to 2020 (Table 2). From 1975–2016 we used the glacier elevation change dataset offered by Maurer et al. [26] (DH/DT_M, hereafter), for 2000–2016 (DH/DT_B, hereafter) by Brun et al. [4], and 2000–2020 (DH/DT_H, hereafter) by Hugonnet et al. [27].

Among the three series of datasets, the DH/DT_M and DH/DT_B have the same pixel resolution of 30 m. The former was derived by fitting robust linear trends to the time series of elevation pixels from KH-9 HEXAGON and ASTER digital elevation models [26], while the latter was acquired from ASTER stereo images [4]. As for the DH/DT_H of 100 m pixel resolution from 2000 to 2020, DH/DT_H is available with five-, ten-, and twenty-year temporal intervals.

3.1.5. Climate Data

For defining glacier accumulation and melting season, ERA5-Land monthly averaged data from 1950 to 1980 [29] and from 1981 to 2021 [28] were downloaded from "https://cds.climate.copernicus.eu/ (accessed on 9 April 2022)." Using the precipitation and air temperature values at 2 m above the land surface, we defined the accumulation season from October to April and the melting or ablation season from May to September.

3.2. Methods

3.2.1. Glacier Outline Extraction

GEE-Based Process

We mapped the glacier coverage and updated the glacier inventory in the Dhauliganga catchment in 2001 and 2020 (Figure 3).

Clean ice has high reflectance in visible bands and low reflectance in the short-wave infrared region. Although the normalized differential snow index (NDSI) has a clear result for mapping, it cannot accommodate errors generated by mountain shadows [37]. On the other hand, the band ratio effectively addresses shadow cover parts and is widely used to delineate debris-free glaciers [37–41]. Therefore, we used the ratio between the red band and short-wave infrared 1 band in the GEE to describe clean ice. The mathematical formula of the band ratio is given in Equation (1).

$$Band\ ratio = \frac{Red}{SWIR1} \quad (1)$$

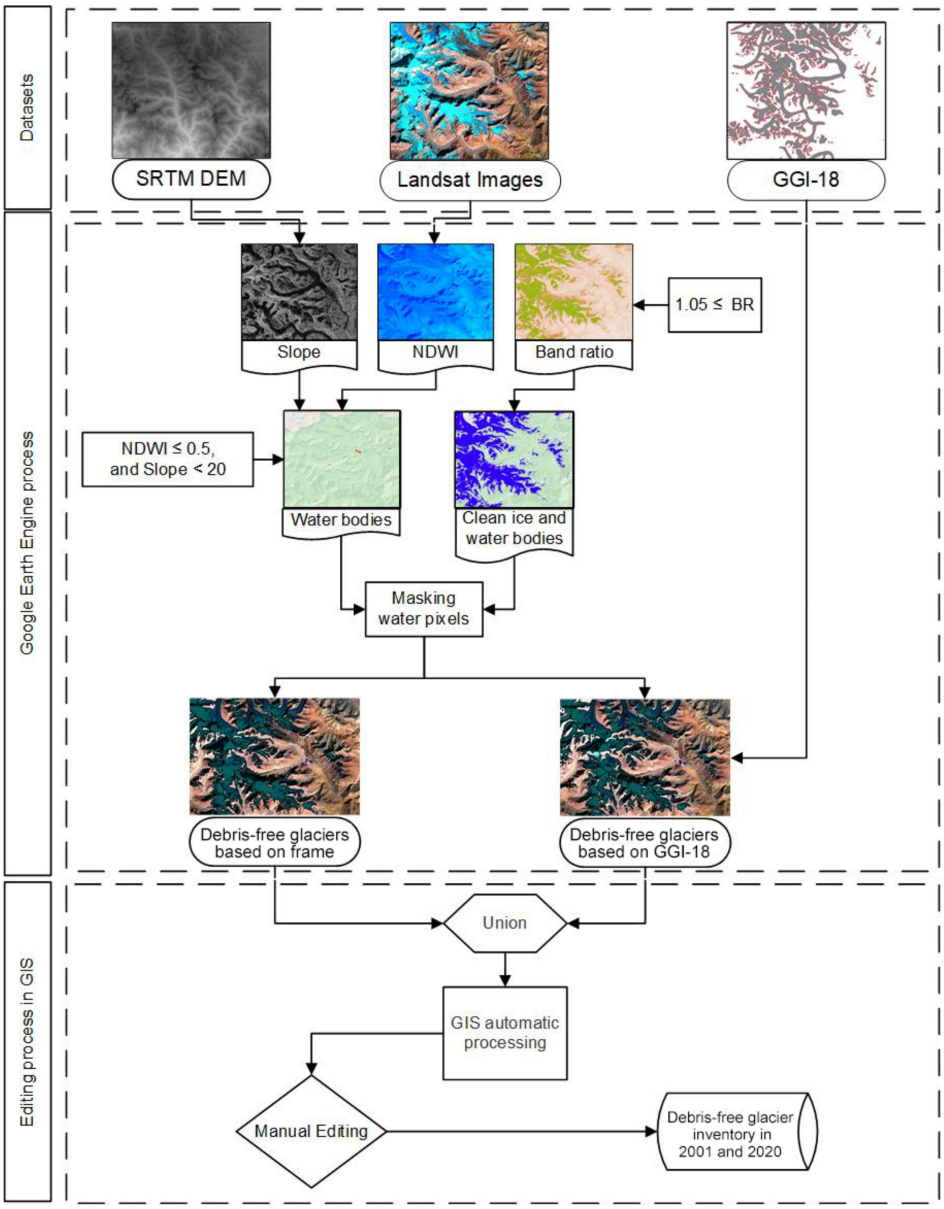

Figure 3. Flow chart of the methodology for the inventories in 2001 and 2020.

where *Red* is the red band (band 4 for Landsat 8 and band 3 for Landsat 7 and 5), and *SWIR*1 is the short-wave infrared 1 band (band 6 for Landsat 8 and band 5 for Landsat 7 and 5). To avoid non-glacier pixels and noise from band ratio results, we applied multiple thresholds ranging from 1.05 to 2. The band ratio values varied with the surface reflectance of a glacier and its surrounding stable ground. Additionally, we used the normalized difference water index (NDWI) with multiple threshold values assigned to mask out water bodies. Equation (2) is the mathematical form of NDWI, derived from the green and near-infrared bands [42].

$$\text{NDWI} = \frac{Green - NIR}{Green + NIR} \tag{2}$$

where *Green* is the green band (band 3 in Landsat 8 and band 2 in Landsat 5 and 7), and *NIR* is near the infrared band (band 5 in Landsat 8 and band 4 in Landsat 5 and 7). Because of the significant effect of glacier lakes on slope gradient, the SRTM digital elevation model V3 product [33] was used to compute the slope. Threshold values for NDWI were $\leq$0.5,

and the slope was fixed at $\leq 20^{\circ}$. After the removal of water pixels, only clean ice pixels remained. Then, the clean ice pixels were transferred into two editable vector files. One is based on the GGI18-18, and the second is the small frame boundary.

Editing Process in GIS

The two exported vector files from GEE were in GEOJSON format. We converted the GEOJSON files into shapefiles and then re-projected them to the "Asia_North_Albers_Equal_Area_Conic" projection system for further processing. The small frame-based shapefiles contain ice patches, not individual glaciers. Therefore, a GGI-18-based shapefile was used to split these ice patches into individual glaciers with the following steps.

(1) Union of both shapefiles.
(2) The "Explode multipart feature" function was then applied so that merged small polygons on the edges could divide into small individual polygons.
(3) We selected polygons with no Glacier ID and areas less than 0.1 km^2 to merge these small polygons with the nearest glacier.
(4) The "Eliminate" function was applied to merge these selected polygons with the nearest glacier polygon.
(5) The "Dissolve" function was applied using Glacier ID to merge the small polygons.
(6) We manually removed the extraneous noise caused by cloud cover and seasonal snow cover.

Mapping Challenges and Solutions

GGI-18 does not contain the GLIMS ID [11], making it challenging to analyze glacier changes and compare them with earlier inventories. Following Raup et al. [43], we calculated glacier-ID by the centroid of each glacier, including its longitude and latitude to three decimals.

When cloud cover made it hard to map glaciers, we replaced that part of the image with a different one from the closest image that had the least snow and cloud cover at that time of year.

A fixed threshold for band ratio for the entire image would cause uncertainties because of the difference in surface reflectance in the adjacent areas of a glacier. Therefore, we selected small frames for similar surface reflectance areas and used multiple threshold values for the same image.

Calculation of Glacier Area Change

We applied the method of Ye et al. [3] to calculate glacier change in terms of physical area ΔA with Equation (3), normalized percentage with AP Equation (4), and change rate AR with Equation (5)

$$\Delta A = A_1 - A_0 \tag{3}$$

$$AP = \frac{\Delta A}{A_0} \times 100 \tag{4}$$

$$AR = \frac{AP}{\Delta t} \tag{5}$$

where A_0 represents the glacier area from an earlier inventory, A_1 represents the glacier area from a later inventory, and Δt is the time interval between the inventories.

3.2.2. Glacier Mass Balance Analysis

Geoid Transformation

Before further processing, all datasets were converted into the "Asia_North_Albers_Equal_Area_Conic" projection system. SRTM-C and NASA DEM were referenced to the EGM96 geoid, whereas SRTM-X, TanDEM-X, and ICESat-2 datasets were referenced to the

WGS84 ellipsoid. Hence, we converted all datasets into EGM96 geoid referencing using Equation (6) to avoid errors from a different referencing system.

$$H = h - N \tag{6}$$

where H is orthometric height, h is ellipsoid height and N Geoid height. To calculate the orthometric height of raster datasets, we used geoid height in raster format with a resolution of 15° downloaded from ("https://www.agisoft.com/downloads/geoids/" (accessed on 17 January 2022). For converting ICESat-2, we used the geoid data provided in the metadata of each ICESat-2 footprint.

Penetration Depth Correction

As SRTM is derived from C-band SAR, the radar signal penetration may reach up to several meters in snow and ice. Therefore, we utilized the SRTM-X band as a reference to determine the penetration depth of the SRTM-C band, similar to previous research [44,45]. Considering the limited coverage of the SRTM-X band in the study area, we selected an extent of 77.50°E, 29.50°N, 82.50°E, and 32.50°N surrounding the study area (Figure 4a) to calculate the SRTM snow penetration.

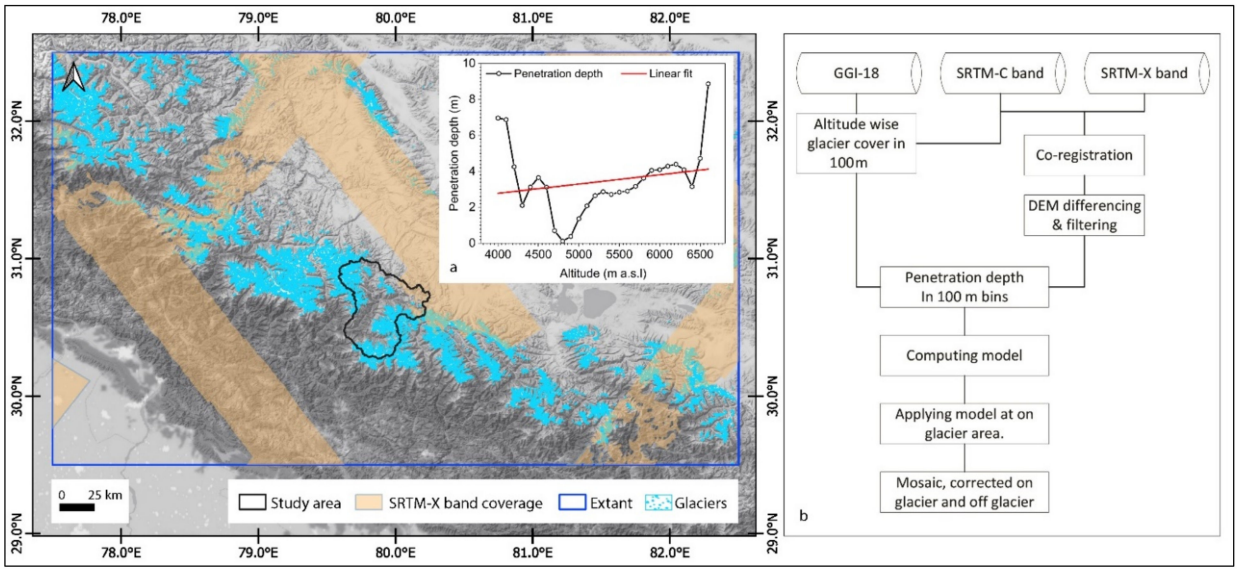

Figure 4. The extent regions for correcting penetration depth of SRTM-C band into the snow. (**a**) Relationship between penetration depth and altitude. (**b**) Flow chart of removing SRTM-C penetration depth into the snow.

The Demcorg tool [46] was used to co-register SRTM-C and SRTM-X bands, calculating the difference and filtering the elevation change data. We obtained the mean penetration depth for each 100 m elevation bin from the difference between the SRTM-X and SRTM-C bands ($dh_{(x\text{-}c)}$). According to Ke et al. [44], snow depth was assumed to be a linear function of altitude. Therefore, we developed a Linear model (y = 0.0008x − 2.8667) from the linear fitting of mean $dh_{(x\text{-}c)}$ for each 100 m altitude bin for the glacier cover area, with the Pearson r value of 0.21 and r square value of 0.04. In February 2000, the study area was 100% snow-covered. Therefore, the linear model was applied to each pixel on the glaciers to obtain the penetration depth for the glacier-covered area. Moreover, we added penetration depth to the SRTM-C band to resolve the penetration error (Figure 4b). Based on the linear model, the maximum penetration depth was found to be 3.34 m, and the minimum was 0.18 m.

Co-Registration

For computing a reliable elevation change from multi-temporal elevation datasets, co-registration is the critical first step [44]. For ICESat-2 ATL06 analysis, we considered ICESat-2 points as master points and NASADEM as slave DEM and conducted the co-registration using the approach of Nuth and Kääb [47] with the tool (https://github.com/WangYuzhe/arcPycor (accessed on 7 April 2022) offered by Wang et al. [48]. For raster-to-raster co-registration, we adopted the Demcorg tool offered by Shean et al. [46] using the mode of Nuth and Kääb [47].

Elevation Differencing

For calculating the elevation change between SRTM, TanDEM-X, NASA DEM, and ICESat-2, we used Equation (7).

$$dh = H_1 - H_0 \tag{7}$$

where dh is the elevation change, H_0 is the elevation of an earlier date while H_1 is the elevation of a later date.

Elevation changes greater than 100 m or less than −100 m were assumed errors and excluded. To calculate the surface elevation changes and geodetic mass balance from TanDEM-X–SRTM and pre-existing elevation difference datasets, 50 m altitude bins were used. Furthermore, a 20 m altitude bin was used to calculate mean surface elevation change and geodetic mass balance derived from ICESat-2 and NASA DEM. The spatial resolution of the datasets explained this difference in altitude bins. Finally, to compute the rate of elevation change per year, we used Equation (8).

$$dh/dt = \frac{dh}{T_1 - T_0} \tag{8}$$

where dh/dt is the rate of glacier surface elevation change, T_0 is the date of acquisition of H_0, and T_1 is the date of acquisition of H_1.

For calculating the mean rate of elevation change over the catchment, we used Equation (9).

$$DH/DT = \frac{\sum_1^n (a \times b)}{C} \tag{9}$$

where DH/DT is the mean glacier surface elevation change rate in the catchment, a is the mean dh/dt of a specific altitude bin, b is the number of glacier pixels in the altitude bin, n is the number of altitude bins in the catchment, and C is the total number of glacier pixels in the area.

Glacier Mass Balance Calculation

GAMDAM glacier inventory 2018 [11] was considered as the reference glacier inventory for analyzing glacier surface elevation change and geodetic mass balance. To calculate the geodetic mass balance (MB), in meters of water equivalent per annum (w.e.a^{-1}) from DH/DT, we assumed the glacier bulk density of 850 ± 60 kg m^{-3} proposed by Huss [49]. To obtain the total annual mass change in terms of Gt. a^{-1}, we use Equation (11).

$$MB = DH/DT \times \rho/1000 \tag{10}$$

$$MC = \frac{MB \times A}{1,000,000,000} \tag{11}$$

where A is the glacier-covered area, MB is the geodetic mass balance, ρ is the glacier bulk density, and MC is the total annual glacier mass change.

3.2.3. Uncertainty Assessment

Glacier Area

Uncertainty in glacier mapping attributes to seasonal snow, mountain shadow, cloud cover, variation in the registration and co-registration of images, and manual digitization [3]. Here we estimated the glacier area uncertainty by applying the outline buffer approach similar to previous studies [3,50,51], i.e., using a buffer of glacier outlines equal to half of a pixel (15 m) with Equation (12).

$$A_{err} = \frac{BA}{TA + BA} \times 100 \tag{12}$$

where A_{err} is the glacier area uncertainty, BA is the buffer area, and TA is the total glacier area.

Elevation Change

Elevation change can be affected by radar penetration and glacier area. Assuming stable terrain as 100 m away from glacier polygons, we divided it into 50 m elevation bins. Then, elevation uncertainty on stable terrain was calculated using Equation (10).

Mass Balance Change

The glacier mass balance results are often influenced by errors associated with glacier area, elevation change, penetration depth, density assumption, and random noise [4,44]. Therefore, we calculated the uncertainty in glacier mass balance by the conventional error propagation procedure [52] with Equation (13), an empirical formula.

$$\sigma_{\Delta M} = \sqrt{\sigma_{\Delta h}^2 \times \rho^2 + \sigma_{\rho}^2 \times \Delta h^2} \tag{13}$$

where $\sigma_{\Delta M}$ is total glacier mass balance uncertainty, $\sigma_{\Delta h}$ is the uncertainty of glacier elevation change, and σ_{ρ} uncertainty is related to glacier density. The density uncertainty is 60 kg m^{-3} [49].

4. Results and Discussion

4.1. Glacier Area

4.1.1. Uncertainty Assessment in Glacier Area

Calculated using the outline buffer method, the uncertainties of the total glacier area in 2001 and 2020 were 6.87% and 7.96%, respectively (Table 4). The lengthening outlines caused by broken glaciers in 2020 led to higher uncertainty.

Table 4. Uncertainty assessment of different glacier inventories.

Glacier Inventory	Total Glacier Area (km^2)	Buffer Area (km^2)	Glacier Area Uncertainty (%)
NGI2001	477.47	35.23	6.87%
NGI2020	418.52	36.18	7.96%
TPG2018	297.40	19.58	6.18%
RGI6.0	436.24	26.02	5.63%
GGI-18	518.50	34.06	6.16%

In addition, we compared NDG 2001 with the manually digitized GGI-18 [11] in three sites (Figure 5), given that the glaciers were delineated using the same image in both inventories. This showed that our results of debris-free glaciers from band ratio methods in NDG 2001 are more accurate than the manual digitization in GGI-18.

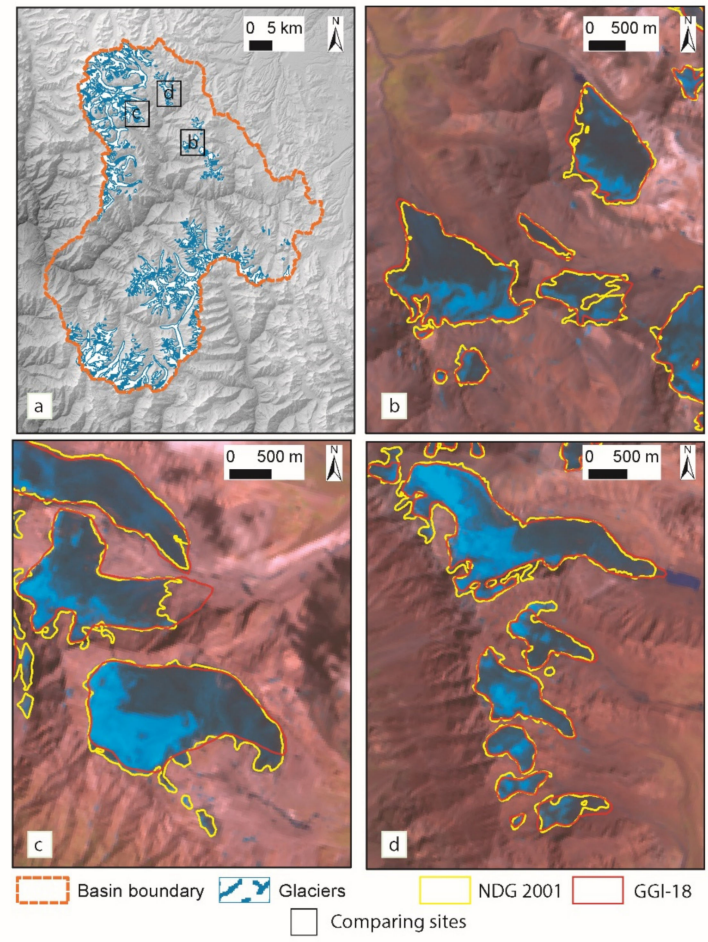

Figure 5. Accuracy assessment of the band ratio results in NDG2001 compared with the manually digitized GGI-18. (**a**) Location of the three sites (**b**–**d**) in the study catchment. The Landsat 7 ETM+ image in the background was on 8 October 2001 (RGB: 543).

4.1.2. Glacier Area Change

We mapped nearly 413 glaciers in the catchment between 2001 and 2020 and analyzed the glacier area change at basin and altitude levels. As a result, the glacier area decreased from 477.47 ± 35.23 km^2 in 2001 to 418.52 ± 36.18 km^2 in 2020, losing an area of 58.95 km^2 within two decades (Table 5). Consequently, the debris-free glaciers covered 16% of the catchment area in 2001 but just 14% in 2020.

Table 5. Total Glacier area change in the catchment from 2001 to 2020 and comparison with previous inventories.

Glacier Inventories (A_1–A_0)	A_0 (km^2)	A_0 (%)	A_1 (km^2)	A_1 (%)	ΔA (km^2)	AP (%)
NDG2020–NDG2001	477.47	16%	418.52	14%	–58.95	–12%
NDG 2020–TPG 2018	297.40	10%	418.52	14%	121.12	41%
NDG2020–GGI-18	518.50	18%	418.52	14%	–99.98	–19%
NDG2020–RGI 6.0	436.24	15%	418.52	14%	–17.72	–4%
TPG 2018–NDG 2001	477.47	16%	297.40	10%	–180.07	–38%
GGI-18–NDG2001	477.47	16%	518.50	18%	41.03	9%
RGI 6.0–NDG2001	477.47	16%	436.24	15%	–41.23	–9%

The glaciers had been shrinking in all directions, especially at the glacier terminus (Figure 6a). A sharp decline in glacier area was detected from 4000 m a.s.l. to 5100 m a.s.l.

(Figure 6b). From 5100 m a.s.l. to 7000 m a.s.l. glacier area loss was decreasing. From 7000 m a.s.l. up to 7700 m a.s.l., there was a nearly balanced area change. The maximum area loss of approximately 3 km^2 occurred around 5100 m a.s.l.

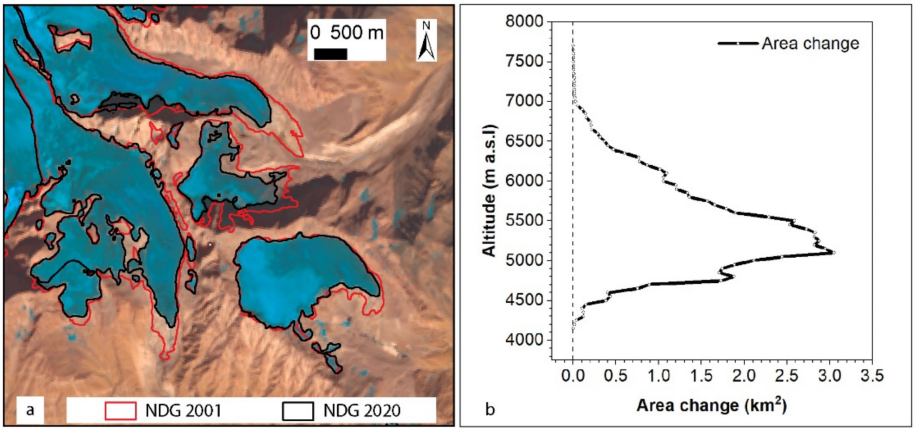

Figure 6. Glacier area change from 2001–2020. (**a**) The shrinking glaciers on Landsat 8 OLI image dated 16 October 2020 (RGB: 654). (**b**) Glacier area changes by altitude in the catchment.

The total glacier area coverage and percentage in the Dhauliganga catchment and the comparison to other glacier inventories, including TPG 2018, RGI 6.0, and GGI-18, are shown in Table 5 and Figure 7. Since our primary aim was to record and analyze the status of glaciers in the Dhauliganga catchment, we mapped only debris-free glaciers while ignoring the debris-covered glaciers. Therefore, the total glacier area was minimized. Except for TPG 2018, previous glacier inventories included debris-covered glaciers, so they reported a more extensive glacier area coverage than ours. For example, NDG 2020 covered 10% more area than TPG 2018 (Table 5).

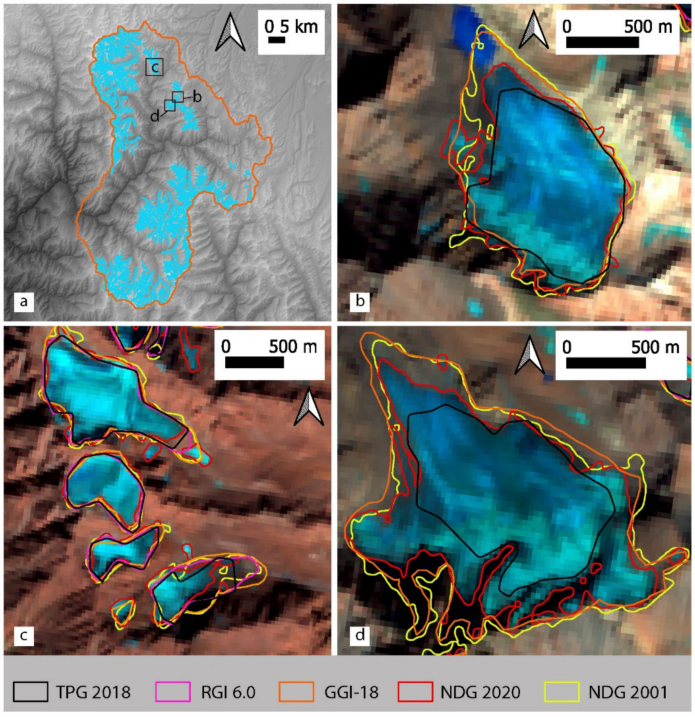

Figure 7. Three examples for comparison of different glacier inventories. (**a**) Location of the three sites (**b**–**d**) in the study catchment. The Landsat 8 OLI image in the background was on 16 October 2020 (RGB: 654).

GGI-18 had the glacier areas (involving debris-covered ice) from 1999 to 2001, with a 9% difference from our inventory of NDG2001 within a similar period. Although our inventory of NDG2001 did not involve debris-covered glaciers, more accurate glacier outlines filled some gaps in glacier areas with GGI-18. Compared with RGI 6.0 from 2001 to 2011, our glacier inventory of NDG 2020 was only 4% less, which presents little difference between them given the glacier change within the period.

4.1.3. Comparison with Other Studies

Comparing the glacier area change in HMA with the Alps [53], Canadian Rockies [54], and Greater Caucasus [55], we can find that the HMA glacier retreat is most remarkable, especially in the Eastern Nyainqentanglha Range of the Southeastern Tibetan Plateau [56] (Table 6). Glacier recession in this part of HMA is comparable and more significant than in the Alps, the Canadian Rockies, and the Greater Caucasus. The minimum glacier area change of HMA glacier recession is located in the Karakoram region [57,58] (Table 6).

In the Central Himalayan region, the glacier recession rates observed by Shangguan et al. [59] and this study were comparable, $-0.49\%\ a^{-1}$ and $-0.65\%\ a^{-1}$, respectively (Table 6). On the other hand, the analysis of Tielidze et al. [55] revealed that the glacier recession rate in the Greater Caucasus was $-1.16\%\ a^{-1}$ from 2000 to 2020, which is twice that of the Dhauliganga catchment in this study (e.g., $-0.65\%\ a^{-1}$) in nearly identical temporal coverage.

Table 6. Comparison of glacier area change in different regions.

Specific Areas	Regions	Time Interval	Glacier Area Change (km^2)	Glacier Area Change (%)	Glacier Area Change Rate (%a^{-1})	Source
Alps	Alps	2003–2015/16	–300	–15%	–1.30%	[53]
Columbia Icefield	Canadian Rockies	1985–2018	–42.56	–18%	–1.10%	[54]
Greater Caucasus	Greater Caucasus	2000–2020	–320.6	–23.2%	−1.16%	[55]
Western Lenglongling Mountains	Northeastern Tibetan Plateau	1972–2007	–24.4	–28.30%	–0.81%	[60]
Eastern Nyainqentanglha Range	Southeastern Tibetan Plateau	1975–2013	–3326.26	–37.69%	–1.32%	[56]
Shyok basin,	East Karakoram	1990–2014	–7.8	–0.19%	–0.01%	[57]
Hunza basin	Western Karakoram	1973–2014	–28.86	–1.36%	–0.03%	[58]
Chandra, Bhaga, Miyar, & Parvati	Western Himalaya	1971–2018	–132.8	–10.20%	–0.22%	[61]
Koshi River basin, Central Himalaya	Central Himalaya	1976–2009	–775.4	–19.40%	–0.49%	[59]
Dhauliganga Catchment	Central Himalaya	2001–2020	–58.95	–12.35%	–0.65%	This study

4.2. Elevation Changes and Mass Balance

4.2.1. Elevation and Mass Balance Changes

The result presents that the catchment has experienced significant glacier loss since 1975, with a remarkably increasing glacier loss rate (Table 7). Meanwhile, the spatial

distribution of elevation changes in the catchment is heterogeneous, with a dramatic glacier thinning rate below 5500 m a.s.l. (Figure 8).

Table 7. Surface elevation change from different datasets.

Datasets	Time Period	Mean Elevation Change (m a^{-1})	Geodetic Mass Balance (m w.e.a^{-1})	Mass Balance (Gt a^{-1})	On Glacier Observation	On Glacier Observed Area (%)	Off-Glacier Observation (Stable Terrain)
TanDEM-X-SRTM	2000–2013	–0.32 ± 0.05	–0.27 ± 0.10	–0.12	517.06	100%	700.35
ICESat-2	2000–2018	–0.28 ± 0.09	–0.24 ± 0.005	–0.09	10,724	–	46,706
ICESat-2	2000–2019	–0.31 ± 0.07	–0.27 ± 0.004	–0.10	14,251	–	63,489
ICESat-2	2000–2020	–0.25 ± 0.03	–0.22 ± 0.002	–0.11	15,429	–	48,277
ICESat-2	2000–2021	–0.27 ± 0.09	–0.23 ± 0.005	–0.10	13,074	–	47,800
ICESat-2	2018–2021	–0.26 ± 0.07	–0.22 ± 0.004	–0.10	52,736	–	204,369
DH/DT_B	2000–2016	–0.31 ± 0.0005	–0.26 ± 0.001	–0.12	495.41	96%	1770.58
DH/DT_M	1975–2000	–0.26 ± 0.002	–0.22 ± 0.002	–0.10	176.88	34%	307.95
DH/DT_M	2000–2016	–0.29 ± 0.004	–0.25 ± 0.003	–0.08	300.7	58%	400.55
DH/DT_H	2000–2005	–0.33 ± 0.001	–0.28 ± 0.0001	–0.13	471.3	91%	1702.4
DH/DT_H	2005–2010	–0.34 ± 0.0018	–0.29 ± 0.0001	–0.14	471.3	91%	1702.4
DH/DT_H	2010–2015	–0.32 ± 0.0013	–0.28 ± 0.0001	–0.13	471.3	91%	1702.4
DH/DT_H	2015–2020	–0.33 ± 0.0014	–0.28 ± 0.0001	–0.13	471.3	91%	1702.4
DH/DT_H	2000–2010	–0.33 ± 0.0012	–0.28 ± 0.0001	–0.13	471.3	91%	1702.4
DH/DT_H	2010–2020	–0.33 ± 0.0013	–0.28 ± 0.0001	–0.13	471.3	91%	1702.4
DH/DT_H	2000–2020	–0.33 ± 0.0013	–0.28 ± 0.0001	–0.13	471.3	91%	1702.4

Figure 9a illustrates results from TanDEM-X and SRTM DEM differencing (hereafter $DH/DT_{TanDEM\text{-}X\_SRTM}$) for glacier cover and non-glacier terrain from 2000 to 2013. We observed that the rate of mean elevation changes during 2000–2013 was -0.32 ± 0.05 m a^{-1}, i.e., geodetic mass balance by -0.27 ± 0.10 m w.e.a^{-1}, with annual glacier mass loss of -0.12 Gt. a^{-1} (Table 7). As clearly seen in Figure 8b1, extreme glacier thinning was observed at the higher altitudes around 7000 m a.s.l. to 7300 m a.s.l. Moreover, the extreme positive elevation change occurred at 6950 m a.s.l. Moreover, we detected a remarkable increase in the glacier thinning rate towards the lower elevations (Figure 8b1).

Figure 9b shows the rate of glacier surface elevation difference for glacier cover and non-glacier terrain derived based on all available ICESat-2 footprints from 25 October 2018–20 December 2021, and NASA DEM (DH/DT_{ICE} hereafter). The averaged glacier surface elevation change rate from 2000–2021 was -0.26 ± 0.07 m a^{-1}, equivalent to -0.22 ± 0.005 m w.e.a^{-1} glacier geodetic mass balance, and -0.10 Gt. a^{-1} annual mass change (Table 7). Results suggest that the maximum glacier change rate from 2018–2021 occurred in 2019, where the mean glacier surface elevation change rate was -0.31 ± 0.07 m a^{-1}, the geodetic mass balance was -0.27 ± 0.004 m w.e.a^{-1}, and the annual glacier change was -0.10 Gt. a^{-1} (Table 7). Conversely, we detected the least glacier change rate in 2020, with the mean glacier surface elevation change rate of -0.25 ± 0.03 m a^{-1} and the geodetic mass balance of -0.22 ± 0.002 m w.e.a^{-1}, resulting in an annual glacier change of -0.11 Gt. a^{-1}.

Mean elevation change, mass balance, and annual glacier loss derived from pre-existing elevation difference datasets covering from 1975 to 2020 are summarized in Table 7. The northwestern part of the catchment, with adequate data coverage from DH/DTM, reveals that glacier loss had significantly increased from 1975–2016 (Figure 10b,c). DH/DTM variation shows that the mean glacier surface elevation change, the geodetic mass balance, and the total annual mass change from 1975 to 2000 were -0.26 ± 0.002 m a^{-1}, -0.22 ± 0.002 m w.e.a^{-1}, and -0.10 Gt. a^{-1}, respectively. According to the DH/DT_M from 2000 and 2016, the mean glacier surface elevation change was -0.29 ± 0.004 m a^{-1}, with a geodetic mass balance of -0.25 ± 0.003 m w.e.a^{-1}, and the annual mass change of -0.08 Gt. a^{-1}. Results derived from DH/DT_B revealed that from 2000 and 2016, the mean glacier surface elevation change was -0.31 ± 0.0005 m a^{-1}, the geodetic mass balance was -0.26 ± 0.001 m w.e.a^{-1}, and the annual mass change was -0.12 Gt. a^{-1}. The results of

these two datasets were consistent with our results by -0.26 ± 0.002 m a^{-1} from 2000 to 2019 (Table 7).

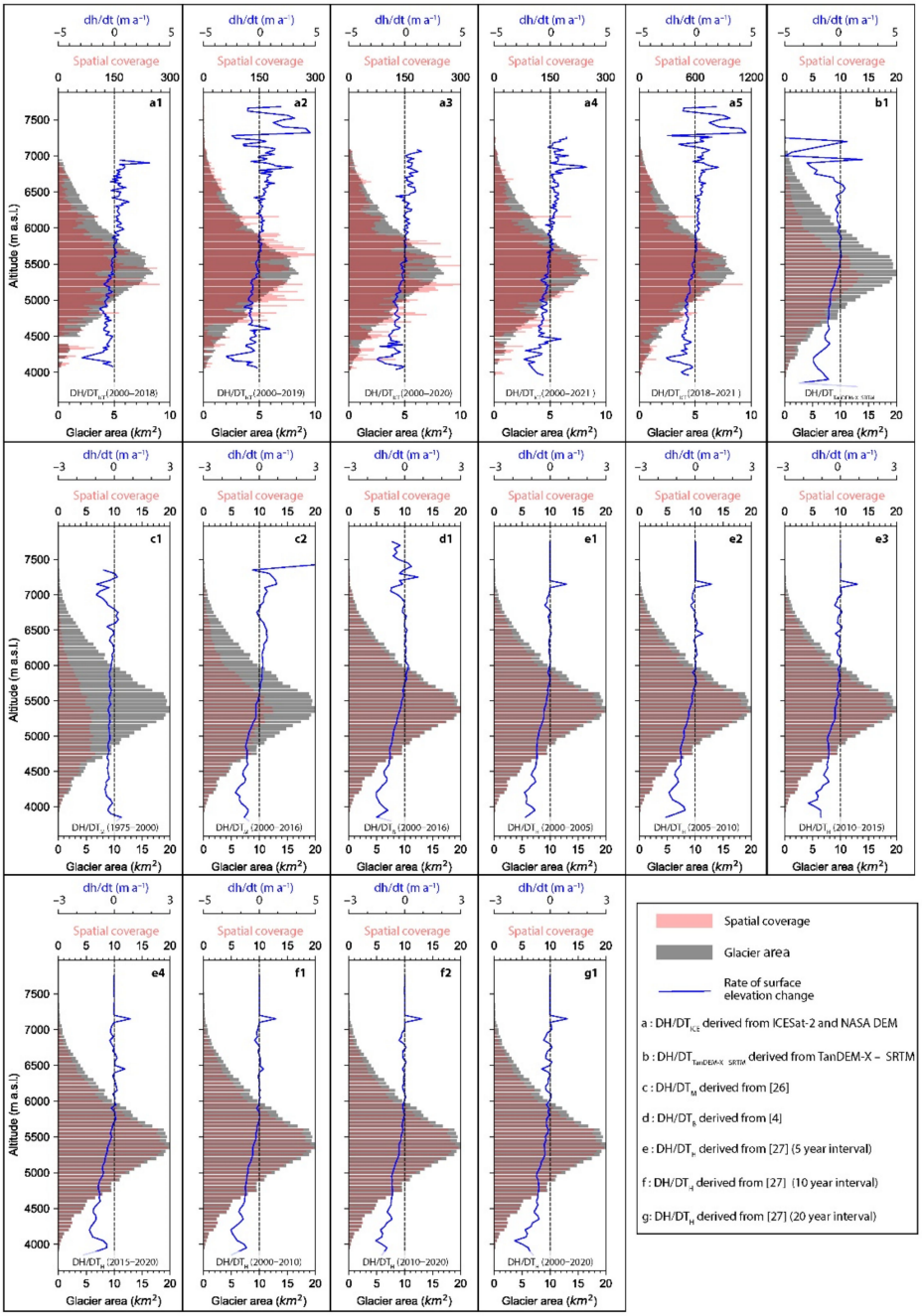

Figure 8. Altitude-dependent distribution of glacier surface elevation change and glacier area from 1975–2021 in the Dhauliganga catchment. (**a1**) DH/DT$_{ICE}$ (2000–2018). (**a2**) DH/DT$_{ICE}$ (2000–2019). (**a3**) DH/DT$_{ICE}$ (2000–2020). (**a4**) DH/DT$_{ICE}$ (2000–2021). (**a5**) DH/DT$_{ICES}$ (2018–2021). (**b1**) DH/DT$_{TanDEM\text{-}X_SRTM}$ (2000–2013). (**c1**) DH/DT$_{M}$ (1975–2000). (**c2**) DH/DT$_{M}$ (2000–2016). (**d1**) DH/DT$_{B}$ (2000–2016). (**e1**) DH/DT$_{H}$ (2000–2005). (**e2**) DH/DT$_{H}$ (2005–2010). (**e3**) DH/DT$_{H}$ (2010–2015). (**e4**) DH/DT$_{H}$ (2015–2020). (**f1**) DH/DT$_{H}$ (2000–2010). (**f2**) DH/DT$_{H}$ (2010–2020). (**g1**) DH/DT$_{H}$ (2000–2020).

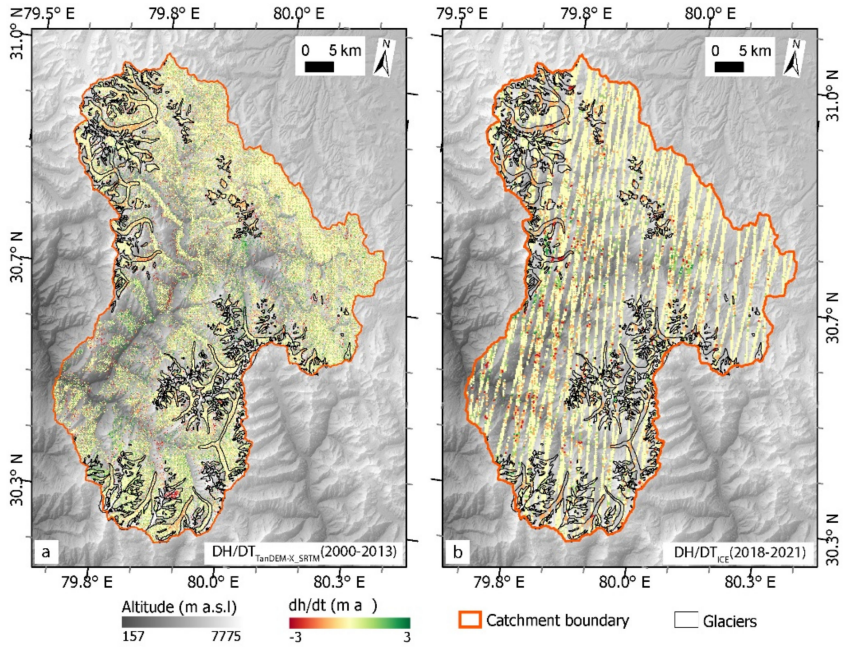

Figure 9. Glacier surface elevation change rate (m a^{-1}). (**a**) Derived from TanDEM-X and SRTM ($DH/DT_{TanDEM\text{-}X\_SRTM}$). (**b**) Derived from ICESat-2 and NASA DEM (DH/DT_{ICE}).

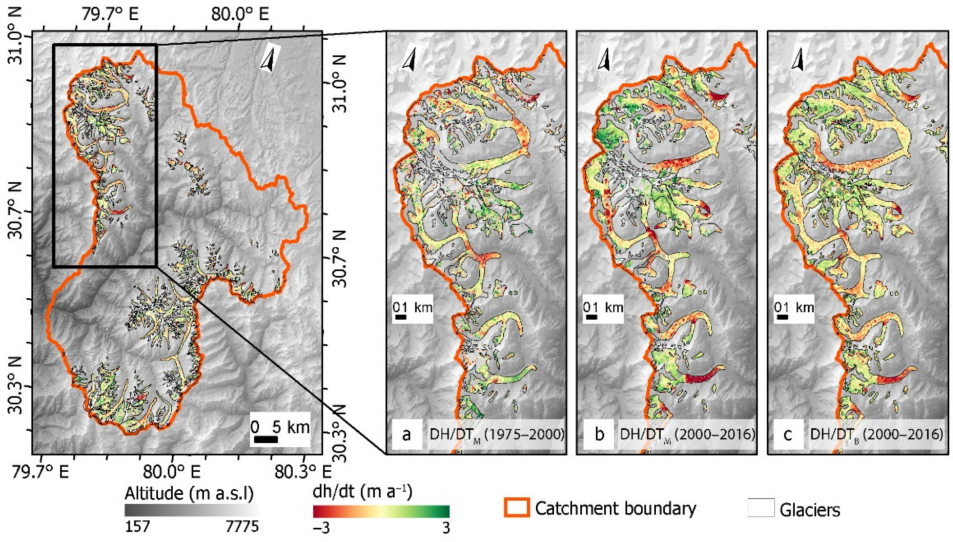

Figure 10. Location of the northwestern catchment for glacier surface elevation change rate (m a^{-1}). (**a**) DH/DT_M (1975–2000). (**b**) DH/DT_M (2000–2016). (**c**) DH/DT_B (2000–2016).

DH/DT_H had a temporal coverage of 2000 to 2020 with five, ten, and twenty-year periods. Elevation change results from DH/DT_H reveal that at higher altitudes, the glacier surface elevation change rate was nearly balanced, except for an altitude of 7150 m a.s.l, with the highest thickening rate (Figure 8e), which is attributed to the suitable altitude range of 7150 m a.s.l. for glacier accumulation. Below the altitude of 5500 m a.s.l., the thinning rate was gradually increasing, although the rate of glacier thinning between 3850 and 4150 m a.s.l varied in different periods (Figure 8).

The estimates of glacier surface elevation change and mass balance based on the DH/DT_{ICE} were slightly less negative than $DH/DT_{TanDEM\text{-}X\_SRTM}$, DH/DT_M, DH/DT_B, and DH/DT_H. The main differences between these datasets were due to spatial coverage, temporal sampling, and elevation measurement uncertainties.

The geodetic mass balance was reported to be -0.22 ± 0.13 m w.e.a^{-1} from 1975 to 2000 and -0.43 ± 0.14 m w.e.a^{-1} from 2000 to 2016 [17]. For western Nepal covering our study area, Zhou et al. [62] reported that the mean glacier elevation change rate decreased at -0.5 m a^{-1} [62]. Brun et al. [4] suggested that the western Nepal region experienced -0.34 ± 0.09 m w.e.a^{-1} from 2000 to 2016. A report from Bandyopadhyay et al. [63] showed that Uttarakhand glaciers had a mean rate of glacier surface elevation change of -0.68 ± 0.01 m a^{-1}, whereas the overall elevation change in fourteen years (2000–2013) was -12.02 ± 1.05 m for the Dhauliganga catchment. Converting the elevation change into elevation change per year, it should be -0.85 ± 1.05 m a^{-1}, while our study reported -0.32 ± 0.05 m a^{-1} elevation change from 2000 to 2013 (Table 7). The significant difference can be attributed to the fact that Bandyopadhyay et al. [63] used a fixed value of 3.5 m for penetration bias correction of all glaciers in Uttarakhand in the central Himalayas. In contrast, we assumed snow depth was a function of altitude, and we applied the linear model for penetration bias correction.

4.2.2. Typical Individual Glacier Mass Balance

The glacier aspect is one of the non-climatic characteristics that play a crucial role in glacier evolution, as it regulates the windward and leeward slope impacts on snowfall and snow redistribution and influences the amount of direct solar radiation a glacier receives [64,65]. Geodetic mass balance results derived from DH/DT$_H$ with five-year intervals from 2000 to 2020 show that Glacier 1 (Figure 11a) and Glacier 2 (Figure 11b) facing East are showing a decline in geodetic glacier mass balance (Table 8). Conversely, glacier 3 (Figure 11c) facing west, Glacier 4 (Figure 11d), and Glacier 5 (Figure 11e) facing north show an increased geodetic glacier mass balance (Table 8).

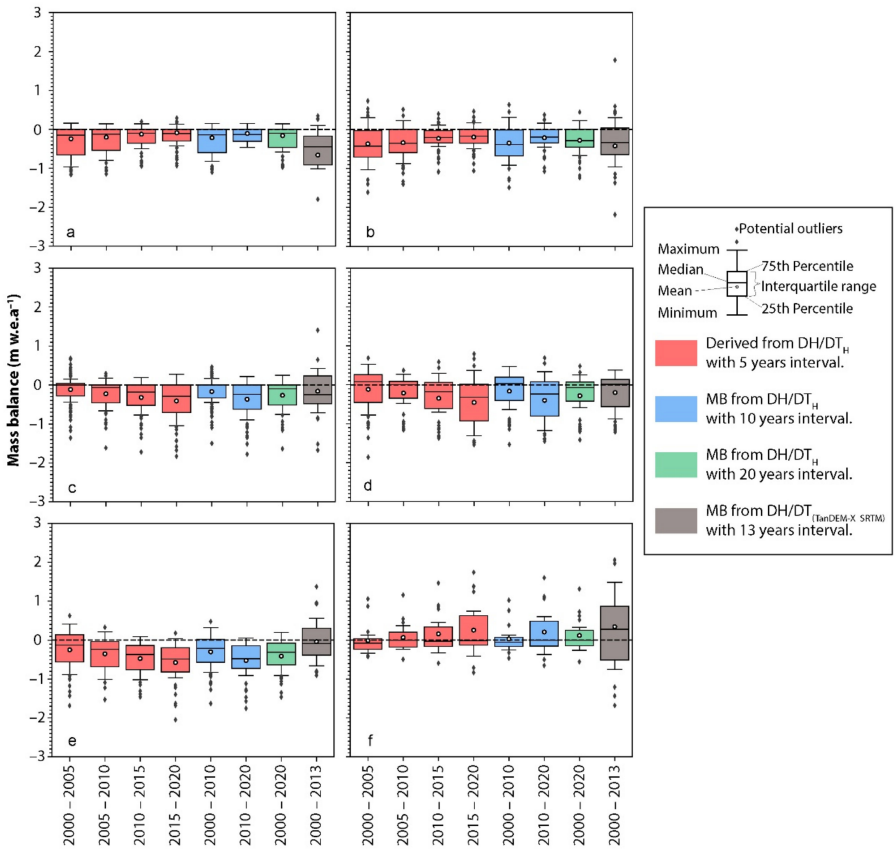

Figure 11. Geodetic mass balance of five selected glaciers for 2000–2020 from DH/DT$_H$ and 2000–2013 from TanDEM-X and SRTM difference. (**a**) Glacier 1. (**b**) Glacier 2. (**c**) Glacier 3. (**d**) Glacier 4. (**e**) Glacier 5. (**f**) Glacier 6 (the collapsed Ronti glacier).

Table 8. Glacier surface elevation change rate (dh/dt), geodetic mass balance (MB), and annual total mass changes (MC) in different periods for the six glaciers.

Glaciers	Change Rate	Time Interval							
		2000–2005	2005–2010	2010–2015	2015–2020	2000–2010	2010–2020	2000–2020	2000–2013
Glacier 1	dh/dt (m a^{-1})	–0.58	–0.51	–0.39	–0.32	–0.54	–0.35	–0.45	–0.58
	MB (m w.e.a^{-1})	–0.49	–0.44	–0.33	–0.28	–0.46	–0.3	–0.38	–0.5
	MC (Gt. a^{-1})	–0.028	–0.025	–0.018	–0.015	–0.026	–0.017	–0.022	–0.029
Glacier 2	dh/dt (m a^{-1})	–0.08	–0.26	–0.46	–0.63	–0.17	–0.54	–0.36	–0.09
	MB (m w.e.a^{-1})	–0.07	–0.22	–0.39	–0.53	–0.14	–0.46	–0.3	–0.08
	MC (Gt. a^{-1})	–0.002	–0.006	–0.011	–0.015	–0.004	–0.013	–0.009	0.000
Glacier 3	dh/dt (m a^{-1})	–0.31	–0.41	–0.61	–0.75	–0.36	–0.68	–0.52	–0.38
	MB (m w.e.a^{-1})	–0.26	–0.35	–0.52	–0.64	–0.3	–0.58	–0.44	–0.32
	MC (Gt. a^{-1})	–0.005	–0.006	–0.01	–0.012	–0.006	–0.011	–0.008	–0.006
Glacier 4	dh/dt (m a^{-1})	–0.56	–0.5	–0.33	–0.27	–0.52	–0.3	–0.41	–0.46
	MB (m w.e.a^{-1})	–0.47	–0.43	–0.28	–0.23	–0.44	–0.26	–0.35	–0.39
	MC (Gt. a^{-1})	–0.021	–0.019	–0.012	–0.01	–0.019	–0.011	–0.015	–0.016
Glacier 5	dh/dt (m a^{-1})	–0.18	–0.37	–0.53	–0.69	–0.27	–0.61	–0.44	–0.29
	MB (m w.e.a^{-1})	–0.16	–0.31	–0.45	–0.58	–0.23	–0.52	–0.37	–0.24
	MC (Gt. a^{-1})	–0.004	–0.01	–0.015	–0.02	–0.007	–0.018	–0.012	–0.006
Glacier 6	dh/dt (m a^{-1})	–0.05	0.08	0.22	0.37	0.01	0.3	0.15	0.31
	MB (m w.e.a^{-1})	–0.04	0.06	0.19	0.32	0.01	0.25	0.13	0.27
	MC (Gt. a^{-1})	–0.00001	0.00007	0.00016	0.00025	0.00003	0.0002	0.00012	0.00021

Glacier 6, which collapsed on 7 February 2021, is facing north. It had a negative geodetic mass balance of −0.04 m w.e.a^{-1} between 2000 and 2005. However, it experienced an increasingly positive mass balance of 0.06 m w.e.a^{-1} from 2005–2010, 0.19 m w.e.a^{-1} from 2010 to 2015, and 0.32 m w.e.a^{-1} from 2015 to 2020 (Figure 11f and Table 8). The steep and high relief of the Ronti peak, the sheared nature of source rock, and contrasting interbedded rock types provided favorable conditions for the glacier to collapse [22]. Furthermore, there was evidence of an earlier event when a piece of ice of approximately 0.16 km^2 broke from the Ronti glacier between 3 January and 8 April 2000 [22].

4.2.3. Seasonal Glacier Analysis of Selected Glaciers Based on ICESat-2

To study the seasonal glacier changes in the selected glaciers, we used ICESat-2 data and NASA DEM. Table 9 shows the mean dh/dt, geodetic mass balance, and total mass change.

Table 9. Glacier surface elevation change rate (dh/dt) and the number of ICESat-2 footprints (Counts) by seasons for five glaciers.

Glaciers	Change Rate	A2018	M2019 [1]	A2019 [1]	M2020	A2020	M2021	A2021
Glacier 1	dh/dt (m a^{-1})	–0.62	–0.27	–0.23	–0.08	–0.65	–0.39	–0.40
	MB (m w.e.a^{-1})	–0.53	–0.23	–0.19	–0.07	–0.55	–0.33	–0.34
	MC (Gt. a^{-1})	–0.018	–0.006	–0.004	0.000	–0.023	–0.013	–0.018
	Counts	1579	538	1105	1170	1157	919	1196
Glacier 2	dh/dt (m a^{-1})	–0.47	–0.38	–0.05	0.06	–0.36	–0.11	–0.09
	MB (m w.e.a^{-1})	–0.40	–0.32	–0.04	0.05	–0.30	–0.09	–0.08
	MC (Gt. a^{-1})	–0.011	–0.005	0.004	0.005	–0.004	–0.002	0.003
	Counts	702	763	722	670	1051	230	1130
Glacier 3 [2]	dh/dt (m a^{-1})	–0.27	–	–0.37	0.47	–0.38	–0.17	–0.30
	MB (m w.e.a^{-1})	–0.23		–0.32	0.40	–0.32	–0.15	–0.25
	MC (Gt. a^{-1})	0.001		–0.002	0.002	–0.012	–0.004	–0.004
	Counts	610		641	42	966	854	465

Table 9. *Cont.*

Glaciers	Change Rate	A2018	M2019 [1]	A2019 [1]	M2020	A2020	M2021	A2021
Glacier 4	dh/dt (m a^{-1})	–0.88	0.01	–0.57	0.58	–0.30	–0.63	–0.16
	MB (m w.e.a^{-1})	–0.75	0.01	–0.48	0.49	–0.25	–0.53	–0.13
	MC (Gt. a^{-1})	–0.002	0.001	–0.002	0.001	–0.002	–0.001	0.003
	Counts	12	183	446	121	282	258	570
Glacier 5 [3]	dh/dt (m a^{-1})	–0.06	1.03	–0.13	–0.35	0.33	–	0.36
	MB (m w.e.a^{-1})	–0.05	0.87	–0.11	–0.30	0.28		0.31
	MC (Gt. a^{-1})	0.001	0.004	0.003	–0.001	0.005		0.001
	Counts	1026	29	456	1243	174		69

[1] A2019 represents the accumulation season in 2019 (October 2018–April 2019), and M2019 was the melting season (May–September) in 2019. [2] For Glacier 3, there were no ICESat-2 footprints in the melting season of 2019. [3] For Glacier 5, there were no ICESat-2 footprints in the melting season of 2021.

The melting rate of Glacier 1 decreased from the accumulation season of 2018 to the melting season of 2020 (Figure 12a). Conversely, the glacier melting rate increased from the melting season of 2020 to the accumulation season of 2020 while decreasing from the accumulation season of 2020 to the accumulation season of 2021 (Figure 12a).

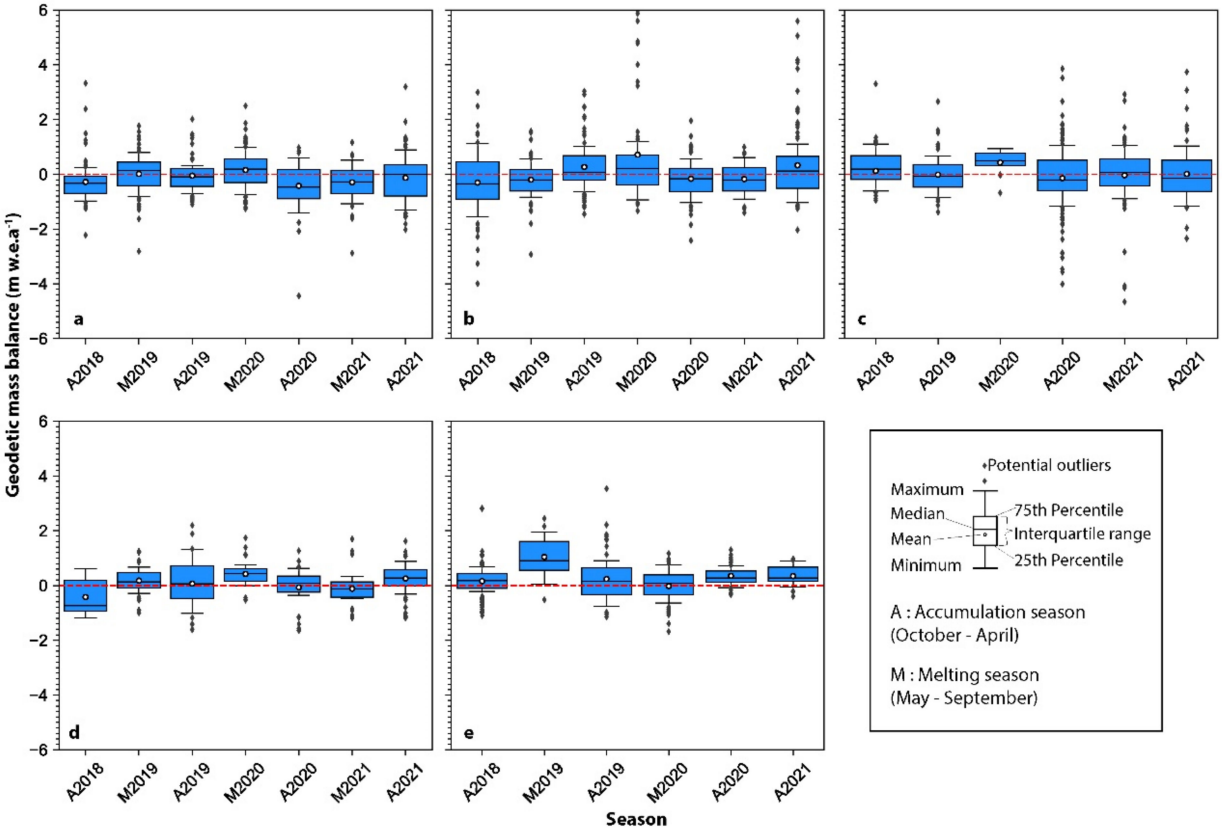

Figure 12. Seasonal geodetic mass balance (m w.e.a^{-1}) for the five selected glaciers derived from ICESat-2 ATL06 footprints and NASA DEM. (**a**) Glacier 1. (**b**) Glacier 2. (**c**) Glacier 3. (**d**) Glacier 4. (**e**) Glacier 5.

Glacier 2 showed a decrease in the rate of glacier melting from the accumulation season of 2018 to the melting season of 2020 (Figure 12b). During the melting season of 2020, a positive geodetic mass balance was detected, but it decreased from the melting season of 2020 to the accumulation season of 2020. Additionally, the glacier melting rate decreased from the accumulation season of 2020 to the accumulation season of 2021 (Figure 12b).

For Glacier 3, there was no ICESat-2 observation for the melting season of 2019. Therefore, glacier 3 had an irregular melting rate pattern, although the maximum melting occurred in the melting season of 2020, with the minimum melting observed in 2021 (Figure 12c).

Similarly, Glacier 4 displayed an irregular pattern, although its maximum melting occurred during the accumulation season of 2018, with a positive mass balance observed during the melting season of 2019 (Figure 12d).

For Glacier 5, there were no ICESat-2 observations for the melting season of 2021. However, positive mass balances were detected for Glacier 5 in the melting season of 2019, the accumulation season of 2020, and the accumulation season of 2021, with the most significant glacier gain in the melting season of 2019 and the least in the accumulation season of 2020 (Figure 12e). Therefore, most glacier melting occurred during the melting season of 2020.

In general, the accumulation season should have a positive glacier mass balance, and the melting season should have a negative mass balance. However, the location of the available ICESat-2 footprints during the respective seasons is the primary explanation for our results of a more negative mass balance during the accumulation season than during the melting season. Figures S1–S5 (Supplementary Materials) illustrate the location of available ICESat-2 footprints over selected glaciers during each accumulation and melting season between accumulation season 2018 and accumulation season 2021. The ICESat-2 footprints we obtained for a particular glacier during the accumulation season are primarily located at lower altitudes with more significant melt (Figures S1–S5 in Supplementary Materials). In contrast, the footprints we obtained during the melting season are mainly located at higher altitudes with less melting (Figures S1–S5 in Supplementary Materials).

5. Conclusions

This study used Landsat images to explore the debris-free glacier area change and available DEMs and ICESat-2 data to examine the glacier surface elevation change rate and geodetic mass balance in India's Dhauliganga catchment over the past two decades. In short, our study improves the understanding of glacier changes in the Dhauliganga catchment in the past several decades. We conclude that ICESat-2 laser altimetry is a practical methodology for studying seasonal glacier dynamics at basin and glacier levels, despite not all glaciers covered by ICESat-2. Furthermore, using state-of-the-art datasets, e.g., ICESat-2 and NASA DEM, helps to improve the accuracy of glacier mass balance estimations in regions with complicated heterogeneous terrain such as HMA.

The catchment lost almost 12.35% of its debris-free glacier area from 2001 to 2020. The area change was spatially heterogeneous, with debris-free area loss having a direct relationship with an increasing altitude between 4000 m a.s.l. and 5100 m a.s.l. and an inverse relationship at elevations higher than 5100 m a.s.l. Moreover, ICESat-2 and NASA DEM-based results from 2000 to 2021 were less negative than other datasets. Glacier mass balance derived from TanDEM-X and SRTM difference from 2000 to 2013 was $-0.27\pm$ 0.10 m w.e.a^{-1}, while it was -0.22 ± 0.004 m w.e.a^{-1} based on ICESat-2 and NASA DEM from 2000 to 2021. We found that the elevation change difference within the two periods was primarily due to the geographical coverage difference between ICESat-2 and other data. Further, the glaciers exhibited an increased glacier thinning rate over the past 45 years. The geodetic mass balance was -0.22 ± 0.002 m w.e.a^{-1} from 1975 to 2000. However, it was up to -0.28 ± 0.0001 m w.e.a^{-1} from 2000 to 2020. Besides, the geodetic study of six individual glaciers disclosed that the two largest east-facing glaciers, Glacier 1 and Glacier 2, were experiencing a declining glacier mass loss. On the other hand, glacier 3 facing the west and Glacier 4 and Glacier 5 facing the north were experiencing an increase in glacier mass loss. Glacier 6, the Ronti glacier, showed a negative mass balance from 2000 to 2005 which then increased positively from 2005 onwards, leading to the devastating Chamoli disaster in India in 2021. Our findings regarding the Ronti glacier highlight the need for

the comprehensive and sustained monitoring of glaciers that are gaining mass to forecast future disasters.

Supplementary Materials: The following supporting information can be downloaded at: https://www.mdpi.com/xxx/s1.

Author Contributions: Conceptualization, Q.Y. and N.A.; methodology, N.A., Q.Y.; software, N.A., X.J.; validation, N.A., X.J. and Y.H.; analysis, N.A.; investigation, N.A., X.J. and Y.H.; resources, X.Z. and L.Z.; data curation, N.A. and A.A.; writing—original draft preparation, N.A. and A.A.; writting—review and editing, X.Z., L.Z. and Q.Y.; visualization, N.A., X.J., Y.H. and A.A.; supervision, Q.Y. and L.Z.; project administration, Q.Y. and L.Z.; funding acquisition, Q.Y. and L.Z.; All authors have read and agreed to the published version of the manuscript.

Funding: The work is supported by the Second Tibetan Plateau Scientific Expedition and Research (STEP, No.2019QZKK0202), the "Strategic Priority Research Program" of the Chinese Academy of Sciences (XDA2002010201, XDA19070302).

Data Availability Statement: The Landsat images are available at "https://earthexplorer.usgs.gov/". The SRTM-C band, NASA DEM and ICESat-2 data are available at "search.earthdata.nasa.gov/". SRTM-X band and TanDEM-X DEMs are available at "https://geoservice.dlr.de/". The processed data and data analysis methods are available upon request.

Acknowledgments: We greatly acknowledge the anonymous reviewers for their valuable comments and suggestions that helped to improve this paper. Bistatic TerraSAR-X/TanDEM-X SAR images in the CoSSC format were provided by the German Aerospace Center (DLR) under project XTI_GLAC6924.

Conflicts of Interest: The authors declare no conflict of interest.

References

1. Consortium, R. *Randolph Glacier Inventory—A Dataset of Global Glacier Outlines: Version 6.0: Technical Report, Global Land Ice Measurements from Space*; RGI Consortium: Boulder, CO, USA, 2017.
2. Yao, T.; Thompson, L.G.; Mosbrugger, V.; Zhang, F.; Ma, Y.; Luo, T.; Xu, B.; Yang, X.; Joswiak, D.R.; Wang, W.; et al. Third Pole Environment (TPE). *Environ. Dev.* **2012**, *3*, 52–64. [CrossRef]
3. Ye, Q.; Zong, J.; Tian, L.; Cogley, J.G.; Song, C.; Guo, W. Glacier changes on the Tibetan Plateau derived from Landsat imagery: Mid-1970s–2000–13. *J. Glaciol.* **2017**, *63*, 273–287. [CrossRef]
4. Brun, F.; Berthier, E.; Wagnon, P.; Kaab, A.; Treichler, D. A spatially resolved estimate of High Mountain Asia glacier mass balances from 2000 to 2016. *Nat. Geosci.* **2017**, *10*, 668–673. [CrossRef] [PubMed]
5. Gardner, A.S.; Moholdt, G.; Cogley, J.G.; Wouters, B.; Arendt, A.A.; Wahr, J.; Berthier, E.; Hock, R.; Pfeffer, W.T.; Kaser, G.; et al. A Reconciled Estimate of Glacier Contributions to Sea Level Rise: 2003 to 2009. *Science* **2013**, *340*, 852–857. [CrossRef]
6. Jakob, L.; Gourmelen, N.; Ewart, M.; Plummer, S. Spatially and temporally resolved ice loss in High Mountain Asia and the Gulf of Alaska observed by CryoSat-2 swath altimetry between 2010 and 2019. *Cryosphere* **2021**, *15*, 1845–1862. [CrossRef]
7. Pritchard, H.D. Asia's shrinking glaciers protect large populations from drought stress. *Nature* **2019**, *569*, 649–654. [CrossRef]
8. Richardson, S.D.; Reynolds, J.M. An overview of glacial hazards in the Himalayas. *Quatern. Int.* **2000**, *65*, 31–47. [CrossRef]
9. Guo, W.; Liu, S.; Xu, J.; Wu, L.; Shangguan, D.; Yao, X.; Wei, J.; Bao, W.; Yu, P.; Liu, Q.; et al. The second Chinese glacier inventory: Data, methods and results. *J. Glaciol.* **2017**, *61*, 357–372. [CrossRef]
10. Nuimura, T.; Sakai, A.; Taniguchi, K.; Nagai, H.; Lamsal, D.; Tsutaki, S.; Kozawa, A.; Hoshina, Y.; Takenaka, S.; Omiya, S.; et al. The GAMDAM glacier inventory: A quality-controlled inventory of Asian glaciers. *Cryosphere* **2015**, *9*, 849–864. [CrossRef]
11. Sakai, A. Brief communication: Updated GAMDAM glacier inventory over high-mountain Asia. *Cryosphere* **2019**, *13*, 2043–2049. [CrossRef]
12. Shi, Y.; Liu, S.; Ye, B.; Liu, C.; Wang, Z. *Concise Glacier Inventory of CHINA*; Shanghai Popular Science Press: Shanghai, China, 2008; pp. 145–146.
13. Sharma, A.; Singh, S.; Kulkarni, A. Glacier inventory in Indus, Ganga and Brahmaputra basins of the Himalaya. *Natl. Acad. Sci. Lett.* **2013**, *36*, 497–505. [CrossRef]
14. Bolch, T.; Kulkarni, A.; Kaab, A.; Huggel, C.; Paul, F.; Cogley, J.G.; Frey, H.; Kargel, J.S.; Fujita, K.; Scheel, M.; et al. The State and Fate of Himalayan Glaciers. *Science* **2012**, *336*, 310–314. [CrossRef]
15. Jacob, T.; Wahr, J.; Pfeffer, W.T.; Swenson, S. Recent contributions of glaciers and ice caps to sea level rise. *Nature* **2012**, *482*, 514–518. [CrossRef]
16. Wang, Q.; Yi, S.; Sun, W. Continuous Estimates of Glacier Mass Balance in High Mountain Asia Based on ICESat-1,2 and GRACE/GRACE Follow-On Data. *Geophys. Res. Lett.* **2021**, *48*, e2020GL090954. [CrossRef]
17. Maurer, J.; Schaefer, J.; Rupper, S.; Corley, A. Acceleration of ice loss across the Himalayas over the past 40 years. *Sci. Adv.* **2019**, *5*, eaav7266. [CrossRef]

18. Kääb, A.; Treichler, D.; Nuth, C.; Berthier, E. Brief Communication: Contending estimates of 2003–2008 glacier mass balance over the Pamir–Karakoram–Himalaya. *Cryosphere* **2015**, *9*, 557–564. [CrossRef]
19. Hock, R.; Rasul, G.; Adler, C.; Cáceres, B.; Gruber, S.; Hirabayashi, Y.; Jackson, M.; Kääb, A.; Kang, S.; Kutuzov, S. High mountain areas. In *IPCC Special Report on the Ocean and Cryosphere in a Changing Climate*; Intergovernmental Panel on Climate Change: Geneva, Switzerland, 2019.
20. Mishra, A. Changing Climate of Uttarakhand, India. *J. Geol. Geosci.* **2014**, 3. [CrossRef]
21. Pandey, P.; Chauhan, P.; Bhatt, C.M.; Thakur, P.K.; Kannaujia, S.; Dhote, P.R.; Roy, A.; Kumar, S.; Chopra, S.; Bhardwaj, A.; et al. Cause and Process Mechanism of Rockslide Triggered Flood Event in Rishiganga and Dhauliganga River Valleys, Chamoli, Uttarakhand, India Using Satellite Remote Sensing and in situ Observations. *J. Indian Soc. Remote* **2021**, *49*, 1011–1024. [CrossRef]
22. Shugar, D.H.; Jacquemart, M.; Shean, D.; Bhushan, S.; Upadhyay, K.; Sattar, A.; Schwanghart, W.; McBride, S.; Vries, M.V.W.d.; Mergili, M.; et al. A massive rock and ice avalanche caused the 2021 disaster at Chamoli, Indian Himalaya. *Science* **2021**, *373*, 300–306. [CrossRef]
23. Shrestha, A.B.; Steiner, J.; Nepal, S.; Maharjan, S.B.; Jackson, M.; Rasul, G.; Bajracharya, B. Understanding the Chamoli flood: Cause, Process, Impacts, and Context of Rapid Infrastructure Development. Available online: https://www.icimod.org/article/understanding-the-chamoli-flood-cause-process-impacts-and-context-of-rapid-infrastructure-development/?utm_source=Cryosphere&utm_campaign=163e11156b-EMAIL_CAMPAIGN_2020_02_14_10_15_COPY_01&utm_medium=email&utm_term=0_d17c66005e-163e11156b-98079682 (accessed on 22 February 2022).
24. Kumar, V.; Shukla, T.; Mehta, M.; Dobhal, D.P.; Bisht, M.P.S.; Nautiyal, S. Glacier changes and associated climate drivers for the last three decades, Nanda Devi region, Central Himalaya, India. *Quatern. Int.* **2021**, *575*, 213–226. [CrossRef]
25. Raj, K.B.G.; Kumar, K.V. Inventory of Glacial Lakes and its Evolution in Uttarakhand Himalaya Using Time Series Satellite Data. *J. Indian Soc. Remote* **2016**, *44*, 959–976. [CrossRef]
26. Maurer, J.; Rupper, S.; Schaefer, J. *High Mountain Asia Gridded Glacier Thickness Change from Multi-Sensor DEMs. NASA National Snow and Ice Data Center Distributed Active Archive Center, Version 1*; National Snow and Ice Data Center: Boulder, CO, USA, 2018. [CrossRef]
27. Hugonnet, R.; McNabb, R.; Berthier, E.; Menounos, B.; Nuth, C.; Girod, L.; Farinotti, D.; Huss, M.; Dussaillant, I.; Brun, F.; et al. Accelerated global glacier mass loss in the early twenty-first century. *Nature* **2021**, *592*, 726–731. [CrossRef] [PubMed]
28. Muñoz Sabater, J. *ERA5-Land Monthly Averaged Data From 1981 to Present*; Copernicus Climate Change Service (C3S), Climate Data Store (CDS): Frascati, Italy, 2019.
29. Muñoz Sabater, J. *ERA5-Land Monthly Averaged Data from 1950 to 1980*; Copernicus Climate Change Service (C3S), Climate Data Store (CDS): Frascati, Italy, 2021.
30. NASA, Earth Data. *NASADEM Merged DEM Global 1 arc Second V001*; NASA: Washington, DC, USA, 2020.
31. Lachaise, M.; Bachmann, M.; Fritz, T.; Huber, M.; Schweißhelm, B.; Wessel, B. The TanDEM-X Change DEM: The New Temporal DEM of the TanDEM-X Mission. In Proceedings of the 13th European Conference on Synthetic Aperture Radar, online, 29 March 2021–1 April 2021.
32. Wessel, B.; Huber, M.; Wohlfart, C.; Marschalk, U.; Kosmann, D.; Roth, A. Accuracy assessment of the global TanDEM-X Digital Elevation Model with GPS data. *ISPRS J. Photogramm. Remote Sens.* **2018**, *139*, 171–182. [CrossRef]
33. Farr, T.G.; Rosen, P.A.; Caro, E.; Crippen, R.; Duren, R.; Hensley, S.; Kobrick, M.; Paller, M.; Rodriguez, E.; Roth, L.; et al. The Shuttle Radar Topography Mission. *Rev. Geophys.* **2007**, 45. [CrossRef]
34. Werner, M. Shuttle radar topography mission (SRTM) mission overview. *Frequenz* **2001**, *55*, 75–79. [CrossRef]
35. Brunt, K.M.; Neumann, T.A.; Larsen, C.F. Assessment of altimetry using ground-based GPS data from the 88S Traverse, Antarctica, in support of ICESat-2. *Cryosphere* **2019**, *13*, 579–590. [CrossRef]
36. Markus, T.; Neumann, T.; Martino, A.; Abdalati, W.; Brunt, K.; Csatho, B.; Farrell, S.; Fricker, H.; Gardner, A.; Harding, D.; et al. The Ice, Cloud, and land Elevation Satellite-2 (ICESat-2): Science requirements, concept, and implementation. *Remote Sens. Environ.* **2017**, *190*, 260–273. [CrossRef]
37. Pratibha, S.; Kulkarni, A. Decadal change in supraglacial debris cover in Baspa basin, Western Himalaya. *Curr. Sci. India* **2018**, *114*, 792–799. [CrossRef]
38. Alifu, H.; Tateishi, R.; Johnson, B. A new band ratio technique for mapping debris-covered glaciers using Landsat imagery and a digital elevation model. *Int. J. Remote Sens.* **2015**, *36*, 2063–2075. [CrossRef]
39. Alifu, H.; Johnson, B.A.; Tateishi, R. Delineation of Debris-Covered Glaciers Based on a Combination of Geomorphometric Parameters and a TIR/NIR/SWIR Band Ratio. *IEEE J. Sel. Top. Appl. Earth Obs. Remote Sens.* **2016**, *9*, 781–792. [CrossRef]
40. Alifu, H.; Hirabayashi, Y.; Johnson, B.; Vuillaume, J.; Kondoh, A.; Urai, M. Inventory of Glaciers in the Shaksgam Valley of the Chinese Karakoram Mountains, 1970'2014. *Remote Sens.* **2018**, *10*, 1166. [CrossRef]
41. Zhang, M.; Wang, X.H.; Shi, C.L.; Yan, D.J. Automated Glacier Extraction Index by Optimization of Red/SWIR and NIR/SWIR Ratio Index for Glacier Mapping Using Landsat Imagery. *Water* **2019**, *11*, 1223. [CrossRef]
42. McFeeters, S.K. The use of the Normalized Difference Water Index (NDWI) in the delineation of open water features. *Int. J. Remote Sens.* **1996**, *17*, 1425–1432. [CrossRef]
43. Raup, B.; Racoviteanu, A.; Khalsa, S.J.S.; Helm, C.; Armstrong, R.; Arnaud, Y. The GLIMS geospatial glacier database: A new tool for studying glacier change. *Global Planet Chang.* **2007**, *56*, 101–110. [CrossRef]

44. Ke, L.H.; Song, C.Q.; Yong, B.; Lei, Y.B.; Ding, X.L. Which heterogeneous glacier melting patterns can be robustly observed from space? A multi-scale assessment in southeastern Tibetan Plateau. *Remote Sens. Environ.* **2020**, *242*, 111777. [CrossRef]
45. Gardelle, J.; Berthier, E.; Arnaud, Y. Impact of resolution and radar penetration on glacier elevation changes computed from DEM differencing. *J. Glaciol.* **2017**, *58*, 419–422. [CrossRef]
46. Shean, D.E.; Alexandrov, O.; Moratto, Z.M.; Smith, B.E.; Joughin, I.R.; Porter, C.; Morin, P. An automated, open-source pipeline for mass production of digital elevation models (DEMs) from very-high-resolution commercial stereo satellite imagery. *ISPRS J. Photogramm. Remote Sens.* **2016**, *116*, 101–117. [CrossRef]
47. Nuth, C.; Kääb, A. Co-registration and bias corrections of satellite elevation data sets for quantifying glacier thickness change. *Cryosphere* **2011**, *5*, 271–290. [CrossRef]
48. Wang, Y.; Ye, Q. arcPycor: An open-source automated GIS tool to co-register elevation datasets. *J. Mt. Sci.* **2021**, *18*, 923–931. [CrossRef]
49. Huss, M. Density assumptions for converting geodetic glacier volume change to mass change. *Cryosphere* **2013**, *7*, 877–887. [CrossRef]
50. Das, S.; Sharma, M.C. Glacier changes between 1971 and 2016 in the Jankar Chhu Watershed, Lahaul Himalaya, India. *J. Glaciol.* **2019**, *65*, 13–28. [CrossRef]
51. Molg, N.; Bolch, T.; Rastner, P.; Strozzi, T.; Paul, F. A consistent glacier inventory for Karakoram and Pamir derived from Landsat data: Distribution of debris cover and mapping challenges. *Earth Syst. Sci. Data* **2018**, *10*, 1807–1827. [CrossRef]
52. Ye, Q.H.; Bolch, T.; Naruse, R.; Wang, Y.Z.; Zong, J.B.; Wang, Z.Y.; Zhao, R.; Yang, D.Q.; Kang, S.C. Glacier mass changes in Rongbuk catchment on Mt. Qomolangma from 1974 to 2006 based on topographic maps and ALOS PRISM data. *J. Hydrol.* **2015**, *530*, 273–280. [CrossRef]
53. Paul, F.; Rastner, P.; Azzoni, R.S.; Diolaiuti, G.; Fugazza, D.; Le Bris, R.; Nemec, J.; Rabatel, A.; Ramusovic, M.; Schwaizer, G.; et al. Glacier shrinkage in the Alps continues unabated as revealed by a new glacier inventory from Sentinel-2. *Earth Syst. Sci. Data* **2020**, *12*, 1805–1821. [CrossRef]
54. Intsiful, A.; Ambinakudige, S. Glacier Cover Change Assessment of the Columbia Icefield in the Canadian Rocky Mountains, Canada (1985–2018). *Geosciences* **2020**, *11*, 19. [CrossRef]
55. Tielidze, L.G.; Nosenko, G.A.; Khromova, T.E.; Paul, F. Strong acceleration of glacier area loss in the Greater Caucasus between 2000 and 2020. *Cryosphere* **2022**, *16*, 489–504. [CrossRef]
56. Ji, Q.; Yang, T.-b.; He, Y.; Chen, J.; Wang, K. Glacier changes in the eastern Nyainqêntanglha Range of Tibetan Plateau from 1975 to 2013. *J. Mt. Sci.* **2016**, *13*, 682–692. [CrossRef]
57. Negi, H.S.; Kumar, A.; Kanda, N.; Thakur, N.K.; Singh, K.K. Status of glaciers and climate change of East Karakoram in early twenty-first century. *Sci. Total Environ.* **2021**, *753*, 141914. [CrossRef]
58. Qureshi, M.A.; Yi, C.; Xu, X.; Li, Y. Glacier status during the period 1973–2014 in the Hunza Basin, Western Karakoram. *Quatern. Int.* **2017**, *444*, 125–136. [CrossRef]
59. Donghui, S.; Shiyin, L.; Yongjian, D.; Lizong, W.; Wei, D.; Wanqin, G.; Yuan, W.; Junli, X.; Xiaojun, Y.; Zhilong, G.; et al. Glacier changes in the Koshi River basin, central Himalaya, from 1976 to 2009, derived from remote-sensing imagery. *Ann. Glaciol.* **2017**, *55*, 61–68. [CrossRef]
60. Pan, B.; Cao, B.; Wang, J.; Zhang, G.; Zhang, C.; Hu, Z.; Huang, B. Glacier variations in response to climate change from 1972 to 2007 in the western Lenglongling mountains, northeastern Tibetan Plateau. *J. Glaciol.* **2017**, *58*, 879–888. [CrossRef]
61. Patel, L.K.; Sharma, A.; Sharma, P.; Singh, A.; Thamban, M. Glacier area changes and its relation to climatological trends over Western Himalaya between 1971 and 2018. *J. Earth Syst. Sci.* **2021**, *130*, 217. [CrossRef]
62. Zhou, Y.; Chen, J.; Cheng, X. Glacier Velocity Changes in the Himalayas in Relation to Ice Mass Balance. *Remote Sens.* **2021**, *13*, 3825. [CrossRef]
63. Bandyopadhyay, D.; Singh, G.; Birajdar, F.J.C.S. Remote sensing analysis of changes in Chorabari glacier, Central Himalaya, India. *Curr. Sci.* **2018**, *114*, 771–775. [CrossRef]
64. Garg, P.K.; Shukla, A.; Jasrotia, A.S. Influence of topography on glacier changes in the central Himalaya, India. *Global Planet Chang.* **2017**, *155*, 196–212. [CrossRef]
65. Patel, L.; Sharma, P.; Fathima, T.; Thamban, M. Geospatial observations of topographical control over the glacier retreat, Miyar basin, Western Himalaya, India. *Environ. Earth Sci.* **2018**, *77*, 190. [CrossRef]